A study of diffuse radio sources from clusters of galaxies

A thesis
submitted to the
Tata Institute of Fundamental Research, Mumbai
for the degree of Master of Philosophy
in Physics
by

Deepak Chandra Joshi

Supervised by

Ruta Kale

National Centre for Radio Astrophysics
Tata Institute of Fundamental Research,
Mumbai

November 2021

Declaration

This thesis is a presentation of my original work. Wherever contributions of others are involved, every effort is made to to indicate this clearly, with due reference to the literature, and acknowledgement of collaborative research and discussions.

This work is done under the guidance of Dr. Ruta Kale at the National Centre for Radio Astrophysics, a centre of the Tata Institute of Fundamental Research, Mumbai.

Deepak Chandra Joshi

In my capacity as supervisor of the candidate's thesis, I certify that the above statement is true to the best of the my knowledge.

Ruta Kale

Date: 18th Nov. 2021.

“ *“The ability to observe without evaluating is the highest form of intelligence.”*

Jiddu Krishnamurti

Synopsis

Clusters of galaxies are the largest gravitationally bound systems in the universe. The intra-cluster medium (ICM) contains, mainly, very hot thermal plasma (detected as X-ray emission). It also contains large scale magnetic fields ($\sim \mu$G) and cosmic rays (relativistic electrons of energies $\sim$ GeV) that elude detection in most frequency bands but manifest as synchrotron sources detectable in radio bands. Mainly massive ($> 5 \times 10^{14}$ $M_{\odot}$) clusters are found to have large scale diffuse radio emission. The large scale diffuse radio sources are broadly classified into radio halos, mini-halos and relics (van Weeren et al., 2019a). Radio halos are found at the centres of clusters while relics are found at the peripheries. Mini-halos are smaller than radio halos and are found in cool-core clusters unlike radio halos and relics that are found in merging clusters. Formation of these diffuse radio sources are not yet well understood. Particle acceleration and magnetic field amplification during cluster mergers have been proposed as mechanisms by which diffuse radio emission is generated in clusters (Brunetti & Jones, 2014a). In this thesis we present radio band studies using the GMRT and VLA of two galaxy clusters aimed at: i) searching diffuse radio emission and ii) finding the nature and origin of the diffuse radio emission.

The galaxy cluster RXC J0528.9-3927 is a bright, massive galaxy cluster at redshift 0.284 that hosts a cool-core and a cold front (Botteon, Gastaldello & Brunetti, 2018). Being a massive cool-core cluster, it was a strong candidate to search for diffuse radio emission. We have carried out a study of the galaxy cluster with the GMRT at 610 MHz. We found that there is a central discrete radio source associated with the Brightest Cluster Galaxy and it is surrounded by diffuse emission. The diffuse emission does not have features typical of jets or lobes of a radio galaxy. The extent of the diffuse source is 197 kpc$\times$ 397 kpc which is typical of radio mini-halos. Botteon, Gastaldello & Brunetti (2018) have found the presence of the cold front in the X-ray observation of the RXC J0528.9-3927 which favours the extended emission to be a mini halo. We used NVSS (1.4 GHz), SUMSS (810 MHz) and TGSS (150 MHz) surveys that covered this cluster but with a lower resolution than our 610 MHz GMRT observations. We assumed that the total flux density in the survey images is the sum of the emission from the central compact source and the extended emission. Assuming a standard spectral index for the compact source, we obtained the flux density of the extended source

at frequencies other than 610 MHz. The integrated spectral index of the mini-halo was found to be -1.9 ± 0.7. The 1.4 GHz radio power of the mini-halo is $6.06 \pm 0.7 \times 10^{25}$ W Hz^{-1}. We compared the radio power with that of the known sample of mini-halos. The central entropy of the cluster falls on the border line between cool-core and non-cool core clusters. Thus this may be a mini-halo in transition to becoming a radio halo. Recently a radio halo has been reported in this cluster using MeeRKAT (Knowles et al., 2021). We compared the properties that we found with those that are reported.

The cluster PLCKESZ G171.94-40.65 was discovered in Sunyaev-Zeldovich observations with the Planck satellite (Planck Collaboration et al., 2011a). A radio halo was discovered in this cluster using the GMRT observations and the NVSS image (Giacintucci et al., 2013). It was speculated that this may be an ultra-steep spectrum radio halo. In this work we analysed deep GMRT and VLA observations of this cluster. We present the images of this cluster with the GMRT at 235, 325 and 610 MHz and VLA D-array at 1-2 GHz. The integrated spectral index of the radio halo is found to be -1.27 ± 0.08. Measurements of total flux densities of radio halos at different frequencies made with radio interferometers are affected by the sensitivity to extended structure of the specific observation. This leads to uncertainties on the spectral indices. Thus a uniform method to find the flux densities of radio halos is needed. Recently the Halo Flux Density Calculator (Halo-FDCA) was proposed to achieve this (Boxelaar, van Weeren & Botteon, 2021). We used it to find the flux density of the halo at 325 MHz and 1400 MHz and compared the values with those found using standard method. We found that the standard method leads to a slightly steeper spectral index as compared to the Halo-FDCA. The radio halo is found to have a standard spectral index and is not an ultra-steep spectrum radio halo. We also found a candidate radio relic having an extent of the 74kpc $\times$ 45kpc. Deep observations will be required to confirm the nature of the candidate relic. We also calculated the equipartition cluster magnetic field to be 3.43 μG.

We assembled a sample of all the radio halos (89) discovered until 2020. The sample until 2019 was taken from van Weeren et al. (2019a) and the sample of remaining newly discovered radio halos are presented in this thesis. We made a sub-sample of radio halos that had measurements at more than one frequency and calculated the spectral indices. We have a total of 33 radio halos in this sub-sample. We explored whether the radio halo spectral indices show any trend

with cluster mass and redshift. More massive clusters may have more powerful mergers and thus may result in flatter spectral indices for radio halos. The inverse-Compton losses increase as a function of redshift and can lead to steepening of radio halos. We did not find any specific correlation between spectral index and mass and between spectral index and redshift. The absence of the trends in these plots can indicate importance of the specific properties of mergers for particle acceleration and the time of observation of the radio halo rather than the total mass or redshift. We also caution about the uncertainty caused by variation in the measurement methods when arriving at total flux densities and spectral indices of the radio halos. We will require uniform multi-frequency measurements to see any specific trend to conclude about the statistical behavior of these large scale diffuse radio sources.

The main outcomes of this thesis are i) the discovery of the radio mini-halo in RXC J0528.9-3927, ii) that the radio halo in PLCKESZ G171.94-40.65 is not an ultra-steep spectrum radio halo, iii) the spectral indices of radio halos show no trend with respect to cluster mass and redshift and iv) uniformity in measurements of the flux densities and spectral indices of radio halos is needed to carry out robust statistical studies.

Acknowledgements

First of all, I convey my heartfelt gratitude to my supervisor Dr. Ruta Kale for her constant support and guidance over the last two years. She encouraged me all the time to explore new things which were beneficial. I would like to thank Dr. Andrea Botteon for providing me the X-ray images of the cluster RXCJ 0528.9-3927. I would also like to thank Dr. Simona Giacintucci for providing the X-ray image of the PLCKG171.9-40.7.

Over the last three years, I have come across many people in NCRA and here I have found a very friendly environment for research work . My batchmates Barun, Shubham, Shyam Sunder and Devojyoti have always supported me.

Finally, I would like to thank all the staff of NCRA and GMRT for making the journey pleasant for me. We have made extensive use of the Numpy, Scipy and Astropy packages and NASA's Astrophysics Data System Bibliographic Services.

This research has made use of the NASA/IPAC Extragalactic Database (NED), which is operated by the Jet Propulsion Laboratory, California Institute of Technology, under contract with the National Aeronautics and Space Administration.

Deepak Chandra Joshi

Pune, November 2021.

Contents

List of Figures

List of Tables

Dedicated to my Parents...

Chapter 1

Introduction to galaxy clusters

Clusters of the galaxies are the most massive collapsed and virialized structures in the universe. These are formed from mergers of small structures in the hierarchical structure formation and evolution model (Zhang, Yu & Lu, 2014) i.e clusters of galaxies form from the largest positive matter density fluctuations. The distribution and evolution of these rare, very large positive density fluctuations are extremely sensitive to the underlying cosmological model. Therefore clusters have been widely used to put constraints on cosmological models. Mergers of small clusters redistribute matter throughout the combined cluster.

A typical cluster of galaxies binds anywhere from hundreds to thousands of galaxies. The masses of these systems are in the range $10^{14} - 10^{15}$ $M_{\odot}$. Galaxy clusters have three main components: 1. galaxies, 2. dark matter (DM), and 3. Intra cluster Medium (ICM). Galaxies share only a small fraction of total mass of cluster and it is about 1%. Dark matter shares a very large fraction of total mass and it is about 90%. The third component, ICM shares about 9% of total mass. In this way we can see that cluster evolution is mostly governed by the DM, but DM only interact via gravity and hence very less information is known about the DM. Most galaxy clusters consist of a Brightest Cluster Galaxy (BCG), whic is the most luminous galaxy in the cluster, generally lying very close to the spatial and kinematical centre of the cluster and it is useful to investigate the dark matter effects in galaxy cluster. When merger takes place DM and galaxies behave as collisionless components. The ICM is composed primarily of ordinary baryons, mainly electrons, ionised hydrogen and helium. This plasma is enriched with heavier elements, including iron. Due to the gravitational field of clusters, metal-enriched

gas ejected from supernovae remains gravitationally bound to the cluster as part of the ICM(Loewenstein, 2004). By looking at clusters across redshifts, which corresponds to looking at different epochs of the evolution of the universe, the ICM can provide a history of element production in galaxies.

Although the ICM on the whole contains the bulk of a cluster's baryons, it is not very dense, with typical values of 10^{-3} particles per cubic centimeter. The mean free path of the particles is roughly 10^{16} m, or about one lightyear. The density of the ICM rises towards the centre of the cluster with a relatively strong peak. When merger of two subclusters takes place, the ICM behaves as a weakly collisional plasma and temperature of the ICM rises due to shocks. Most of the shock energy goes into thermal heating of the ICM. ICM temperature typically drops to 1/2 or 1/3 of the outer value in the central regions. Once the density of the plasma reaches a critical value, enough interactions between the ions ensures cooling via X-ray radiation (Sarazin, 1986). As the ICM is at such high temperatures, it emits X-ray radiation, mainly by the thermal bremsstrahlung process and X-ray emission lines from the heavy elements. These X-rays can be observed using an X-ray telescope and through analysis of this data, it is possible to determine the physical conditions, including the temperature, density, and metallicity of the plasma. Measurements of the temperature and density profiles in galaxy clusters allow for a determination of the mass distribution profile of the ICM through hydrostatic equilibrium modeling.

1.1 Radio band study of galaxy clusters

The radio band study of the clusters of the galaxies is the most important tool to study the non-thermal components, namely, the cosmic rays and magnetic fields, of the ICM. The origin of cosmic rays and magnetic fields is not known well and it likely involves cluster mergers, the most energetic events in the universe that dissipate energy up to order of the 10^{63}ergs. Supernovae in the galaxies in clusters, radio jets and lobes of radio galaxies are the typical sources of synchrotron emission from galaxy clusters that are detectable in radio bands. However there are sources not associated with individual galaxies but are associated with the ICM itself which are not yet fully understood.

1.2 Diffuse radio emission from galaxy clusters

When relativistic electrons gyrates in the μG magnetic field of the ICM then it produces the radio emission that permeate the hot ICM. That is the diffuse radio emission of synchrotron origin. And hence it can be used to trace the relativistic electrons and magnetic fields in the galaxy cluster. These diffuse sources have extents of the order of megaparsec and permeate nerly entire volume of the cluster. Presence of relativistic electrons on such large scales cannot be explained by putting together the jets and lobes of radio galaxies alone. The diffusion time of relativistic electrons is much larger compared to their radiative lifetime. It takes more than the Hubble time to transport relativistic electrons to megaparsec scales via diffusion. Thus acceleration mechanisms that produce relativistic electrons all over the ICM are invoked.

1.2.1 Particle acceleration processes in ICM

1.2.1.1 First order Fermi acceleration

This processes is also known as the diffusive shock acceleration (DSA). In this mechanism the particles cross backward and forward across the shock front as they scatter from magnetic inhomogeneities in the shock down and upstream region. The particle gains additional energies in this process (Axford, Leer & Skadron, 1977, Bell, 1978, Blandford & Ostriker, 1978, Krymskii, 1977).

1.2.1.2 Second order Fermi acceleration

This is a stochastic process where particle accelerates from the magnetic inhomogeneities. In this processes particle can gain or loose energy in scattering. When particle are in random motion the probability for particle to gain energy in a head on collision is slightly higher. As this process is second order in nature, hence it is an inefficient process (Malkov & Drury, 2001, Schlickeiser, Sievers & Thiemann, 1987). Adiabatic compression A shock wave can compress the the bubble /lobe of the old relativistic plasma from an active galactic nucleus. Due to this compression there is an enhancement in the radio synchrotron emission (Enßlin

& Brüggen, 2002, Enßlin & Gopal-Krishna, 2001). This mechanism can lead to revival of old radio galaxy lobes.

1.2.1.3 Secondary models

Another model that can produce the cosmic ray electrons is via secondary particles. According to this model the collision between the relativistic protons and the thermal protons after decay give rise to the secondary electrons (Blasi & Colafrancesco, 1999, Dennison, 1980). However there is arguments against the hadronic model is that there must be gamma rays detection from these sources but so far no such detection have observed. A recent detection towards Coma cluster has been claimed (Adam et al., 2021).

1.2.2 Cluster radio halos

Cluster giant radio halos are the extended diffuse radio sources with low surface brightness that roughly follows the ICM distribution (Fig. 1.1). These sources are not associated with any individual galaxy within the cluster. Most of the radio halos have the steep spectra as compared to radio galaxies and are characterised by regular morphology. These sources show low or negligible polarisation. The typical sizes of these sources is order of the 1 Mpc or more, however there are some with sizes about 700 kpc. Sensitive radio studies suggested that radio halo morphology is correlated with the X-ray structure and shows the indication of the merger processes in two sub clusters, possibly related to halo formation.

The origin of the radio halos is still a matter of the debate. There are two models hadronic and the turbulent re-acceleration. In the hadronic model the radio emitting electrons are a consequence of the collision between the cosmic ray protons and the thermal protons of the ICM (Blasi & Colafrancesco, 1999, Dennison, 1980, Dolag & Enßlin, 2000). In the turbulent re- acceleration model the population of the seed electrons is re- accelerated as a powerful state of the ICM turbulence due to cluster merger (Brunetti et al., 2001, Donnert et al., 2013). However there are arguments against the hadronic model based on the integrated radio radio spectra, spatial characteristic of the radio halos and the radio-X-ray scaling relations. The spatial distribution of the spectral index can vary from the uniform to patchy. High frequency (5GHz) observations of the known radio halos would

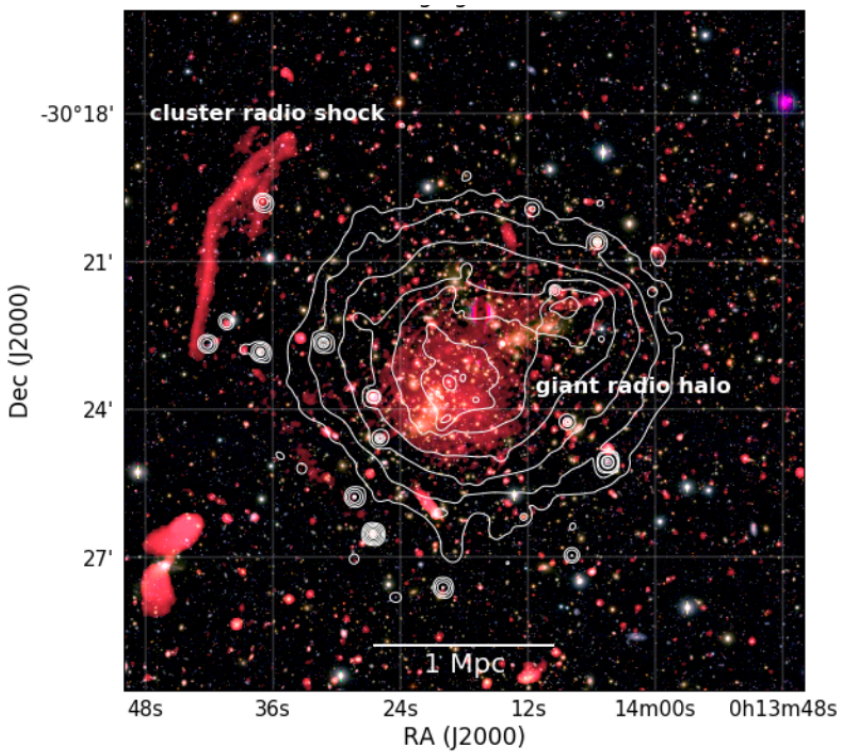

FIGURE 1.1: This is VLA 1.4 GHz image of the merging galaxy cluster Abell 2744 with giant radio halo and cluster radio shocks labeled. Chandra X-ray contours are shown in white. X-ray surface brightness contours are proportional to [1,4,16,64]. (van Weeren et al., 2019b)

enable a search of the possible cutoffs. Nowadays turbulent re-acceleration model is thought to be the main mechanism which is responsible for the origin of the radio halos in galaxy cluster.

While most of the radio halos have spectral indices in the range $-1.0 - -1.4$, the the turbulent re-acceleration model predicted that there could be a population of "ultra-steep spectrum" (USS) radio halos. The first example of an USS radio halo was reported by Brunetti et al. (2008) and subsequently a few such radio halos have been discovered. These radio halos are important to constrain the parameters of the acceleration mechanisms.

1.2.3 Cluster radio relics

The radio relics are similar to the radio halos with low surface brightness and sizes up to 1 Mpc and also shows the steep spectrum but the location of these sources are cluster peripheral regions and morphologies are elongated (Fig. 1.1). Relics

sources are generally arc-like structures and highly polarised ($\sim$ 20%). These sources are also not associated with any individual galaxy in the cluster. The sources are found at the location of the shocks that are detected using X-ray observations. There are still open questions of the underlying re-acceleration process that generates the synchrotron emitting cosmic ray electrons at these shocks.

1.2.4 Radio mini-halos

Radio mini halos are the diffuse extended radio sources which have sizes of 100-500 kpc and are found in relaxed, cool-core clusters, with the radio emission surrounding the brightest cluster galaxy (Fig. 1.2). The sizes of the mini halos are comparable to that of the central cluster cooling regions. The radio emission from the mini-halos does not directly originate from the central AGN. Similar to giant radio halos the hadronic models and turbulent re-acceleration model has been used to explain the presence of the cosmic rays synchrotron emitting electrons. Unlike the giant radio halos where turbulence is due to the major merger, in case of the mini-halos it is due to the minor merger or turbulence in the cluster core regions the due gas sloshing or the AGN jets. The central Active galactic nuclei is likely the source of the fossil electrons that are re-accelerated and produce the mini-halo. The confinement of the mini halos by cold fronts also supports that gas sloshing can re-accelerates the particles (ZuHone et al., 2014).

1.3 Motivation

In this thesis we have undertaken radio band studies of two galaxy clusters and assembled a sample of radio halos for statistical study. We describe the motivation behind each of this study.

The galaxy cluster RXC J0528.9-3927 is a bright, massive galaxy cluster at redshift 0.284 that hosts a cool-core and a cold front (Botteon, Gastaldello & Brunetti, 2018). Clusters in the southern sky remained out of the cluster samples searched for diffuse radio emission for a long time due to the lack of sensitive radio interferometric observations (e. g. Kale et al., 2015, 2013, Venturi et al., 2007, 2008). Simulations of observations with the Giant Metrewave Radio Telescope (GMRT)

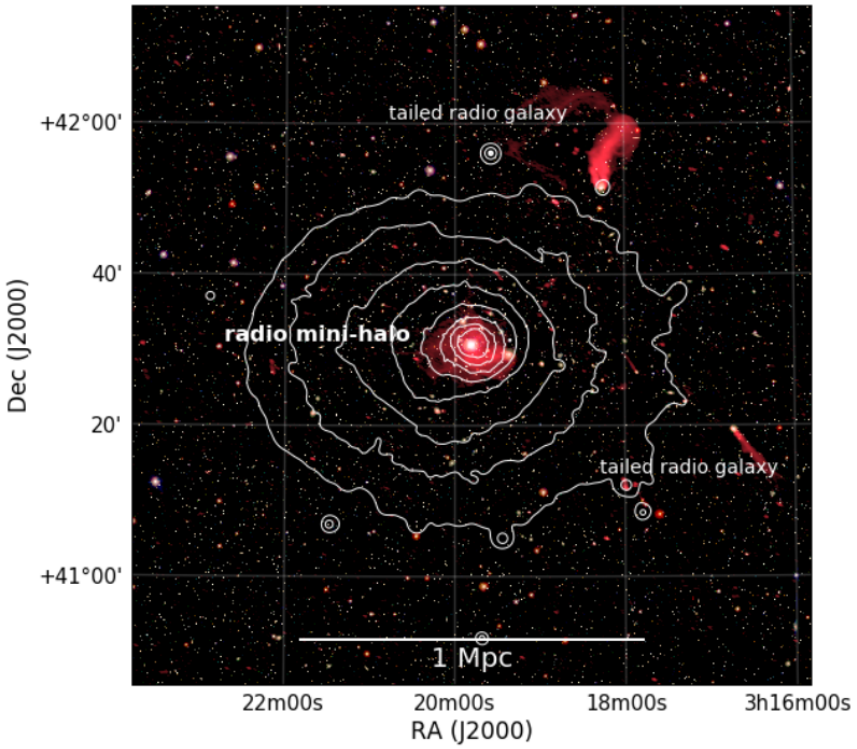

FIGURE 1.2: This VLA 230 -470 MHz image of the relaxed cool core Perseus cluster from (van Weeren et al., 2019b) XMM-Newton X-ray contours in the 0.4-1.3 keV band are overlaid in white with contour spacing proportional to [1, 4, 16, 64].

showed that that for southern declinations the short baseline coverage is better (projected baseline lengths are shorter) and the extended emission can be recovered well even with low elevation observations (Deo & Kale, 2017). RXC J0528.9-3927 was observed with the GMRT as a part of the SoUthern Cluster sCale Extended Source Survey (SUCCESS) sample (PI: R. Kale). Being a massive cool-core cluster, it is a strong candidate to search for diffuse radio emission.

The cluster PLCKESZ G171.94-40.65 was discovered in Sunyaev-Zeldovich observations with the Planck satellite (Planck Collaboration et al., 2011a). A radio halo was discovered in this cluster using the GMRT observations and the NRAO Very Large Array (VLA) Sky Survey 1.4 GHz image (Giacintucci et al., 2013). It was speculated that this may be an USS radio halo. Thus further deep observation with the GMRT and the VLA were recorded and in this work we attempt to answer the question whether this radio halo is an ultra-steep spectrum radio halo.

Measurements of total flux densities of radio halos at different frequencies made with radio interferometers are affected by the sensitivity to extended structure of the specific observation. This leads to uncertainties on the spectral indices. Thus

a uniform method to find the flux densities of radio halos is needed. Recently the Halo Flux Density Calculator (Halo-FDCA) was proposed to achieve this (Boxelaar, van Weeren & Botteon, 2021). We took this newly developed technique to find the flux density of the halo at 325 MHz and 1400 MHz and compared the values with standard methods for the case of PLCKESZ G171.94-40.65. We also report the comparison between the standard method and Halo-FDCA.

A statistical study of radio halos is a useful way to investigate the general behaviour of these large scale systems with host cluster properties. Using the sample available from the literature and updating it, we assembled a sample of 89 radio halos. Of these 33 sources have observations at more than one frequencies. We wanted to explore that whether radio halo spectral indices show any trend with cluster mass and redshift. More massive clusters may have more powerful mergers and thus may result in flatter spectral indices for radio halos. The inverse-Compton losses increase as a function of redshift and can lead to steepening of radio halos. This may lead to steep spectrum radio halos to be preferentially be found in high redshift clusters. We present a study of this sample.

Chapter 2

A radio band study of the galaxy cluster RXC J0528.9-3927

2.1 Introduction

Low frequency observations such as with the GMRT are ideal to search for diffuse radio emission in galaxy clusters. This is due to the availability of short and long baselines at the same time. SoUthern Cluster sCale Extended Source Survey (SUCCESS) was a survey undertaken to search for diffuse sources with the GMRT. RXC J0528.9-3927 was the part of the SUCCESS sample containing 9 clusters. The nine clusters were observed with the GMRT under the proposal codes 31_065 and 32_043 (PI R. Kale). The criteria for choosing these clusters were z<0.3, mass> $5 \times 10^{14} M_{\odot}$ and declination $-50^{\circ} < \delta < -30^{\circ}$. These criteria were particularly chosen because the clusters in the southern sky remain out of the survyed samples for a long time because of the bad coverage of these declinations (e. g. Kale et al., 2015, 2013, Venturi et al., 2007, 2008). It is found that radio halos of sizes half of the largest angular scale implied by the shortest baseline can be recovered above 90% (Deo & Kale, 2017, Wilner & Welch, 1994). It was observed that for southern declinations, the short baseline coverage is better (projected baseline lengths are shorter). A radio halo in one of the SUCESS clusters is reported in (Kale, Shende & Parekh, 2019).

In this work we present a study of the cluster RXC J0528.9-3927. The general properties of the cluster RXC J0528.9-3927 are given in Table 2.1. This is a high

TABLE 2.1: General properties of RXC J0528.9-3927 (Planck Collaboration et al., 2014).

$R.A._{J2000}(hms)$	05 28 52.9
$Dec._{J2000}(dms)$	39 28 18.1
z_{Fe}	0.284
$M_{500}(M_{\odot})$	$(7.40 \pm 0.36) \times 10^{14}$
$K_0(keVcm^2)$	73 ± 14
$T(keV)$	7.2 ± 0.9

mass cluster. The previous study on this cluster is due to Botteon, Gastaldello & Brunetti (2018) . The ICM X-ray emission peaked on the cluster core which is the coldest region in cluster and they report the presence of a cold front with $kT_u = 10.5^{+3.6}_{-1.8}keV$ and $kT_d = 7.2^{+0.9}_{-0.7}keV$. Also recently, Knowles et al. (2021) has observed this cluster using MeerKAT as part of the clusters taken from the massive Sunyaev-Zel'dovich-selected galaxy clusters from ACT.

2.2 GMRT observations

GMRT observation were carried out at frequencies 610 MHz with a bandwidth of the 33 MHz. The cluster was observed for 6 hours with integration time 16.10 seconds.

2.3 Data analysis

GMRT data reduction were done with pipeline CAsa Pipeline-cum-Toolkit Upgraded GMRT data reduction-CAPTURE (Kale & Ishwara-Chandra, 2021). CAPTURE flags the bad data (bad channels, bad timeintervals,bad antenna also flags the signals which comes out due to the radio frequency interference with local radio communaications (RFI)). After initial flagging it performs the calibration (fluxscale, delay, bandpass) and then finally performs imaging. Flux calibration is performed using standard flux scale of Perley-Butler 2017 (Perley & Butler, 2017). Self-calibration with phase only and finally with amplitude and phase solutions worked out for six iterations. We have chosen robust= 0 for imaging.

The visibilities after self-calibration were reimaged with choice of lower limit on the uv range to separate out the contribution of the point sources. We first created an image of point sources using a lower cut off for the uv-range 4kλ and weighting scheme briggs. The corresponding model was subtracted from the calibrated visibilities. We then create the final image with this visibility file using the uvrange $< 8k\lambda$. All imaging was done with CASA task tclean and multi-frequency-synthesis (MFS) algorithm with two Taylor term(nterms= 1) to model the frequency dependence. We have used the gridder=wproject for widefield correction with wprojection planes= 256. We automated this process by writing a python script.

2.4 Results

2.4.1 Radio images

We have shown the radio robust zero image of the galaxy cluster RXC J0528.9-3927 and the zoomed view of the central source in Fig. 2.1. The restoring beam 7.5"×4.6" with P.A at 15.92°. We have shown the zoomed view of the source of the interest on the bottom of the image. The r.m.s of the image is 43μJy/beam. The positive contours are shown in green are 6σ, 12σ, 24σ, 48$\sigma$and 96σ. We have detected a candidate diffuse radio emission in the galaxy cluster. In Fig. 2.2 shown the point source subtracted image of the cluster with presence of the diffuse emission in it. In Fig. 2.2 we have shown the X-ray surface brightness image of the galaxy cluster with radio contours overlaid on it to see the radio and X-ray surface brightness correlation. In Fig. 2.3 we have shown the temperature map overlaid with radio contours of the galaxy cluster as temperature gives us the information about the merger history. Red arc shows the location of the cold front. In Fig. 2.4 we have shown the entropy map for the galaxy cluster overlaid with radio contours. Entropy map gives us information about the measure of the disturbance that takes place due to the merger, and its measures differ for differ diffuse radio emission.

2.4.2 BCG radio spectrum

We have GMRT observation at 610 MHz. We have analysed the GMRT data at this frequency to get the flux density. The total flux density $F_\nu$total was measured

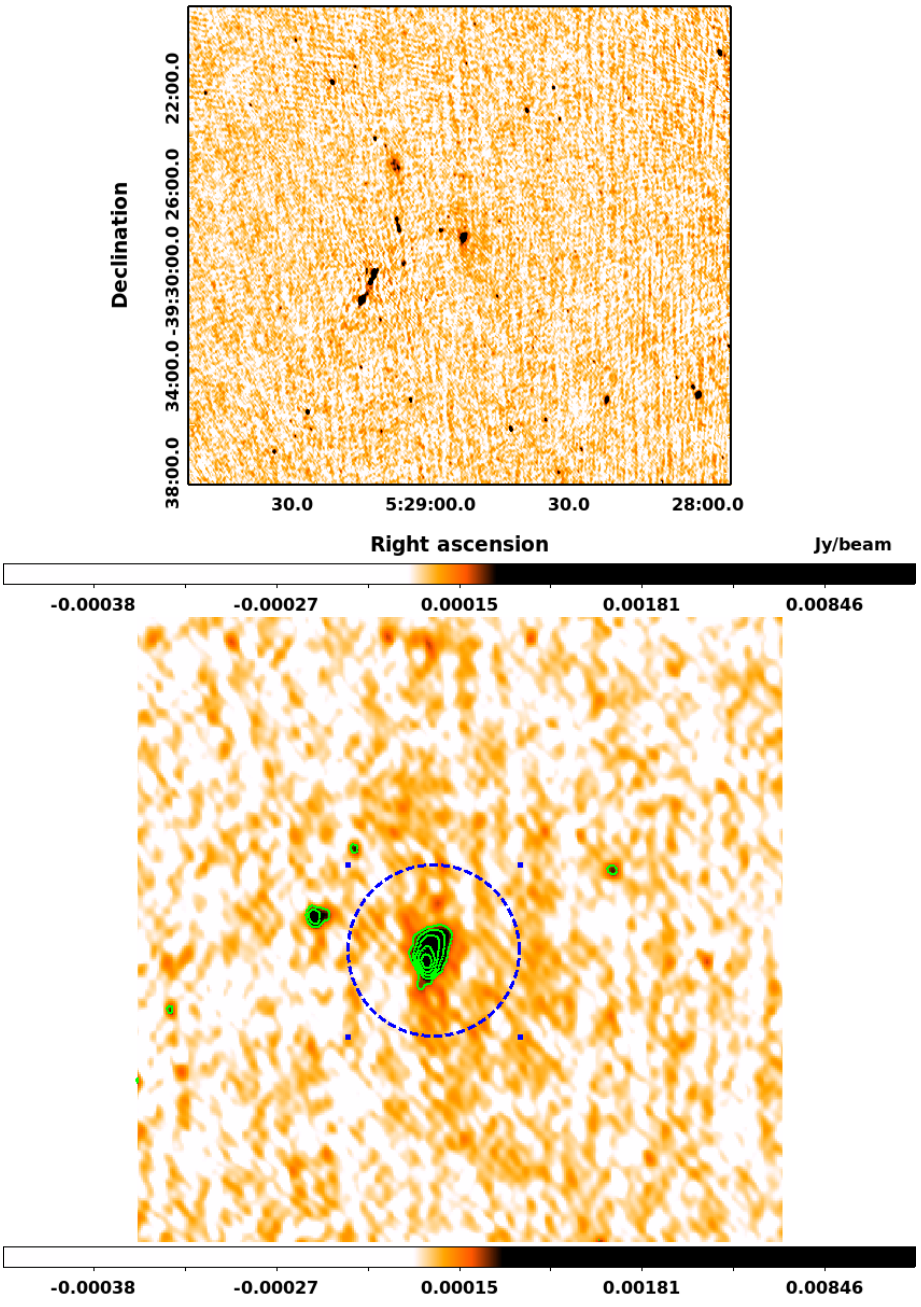

FIGURE 2.1: This is robust 0 GMRT 610MHZ image of the RBS 0653 with restoring beam 7.5"×4.6" with P.A at 15.92°.We have shown the zoomed view of the source of the interest on the bottom of the image.The r.m.s of the image is 43μJy/beam.positive contours are shown in green are 6σ,12σ,24σ,48$\sigma$and 96σ. The bottom figure has also the colorbar with (Jy/beam).

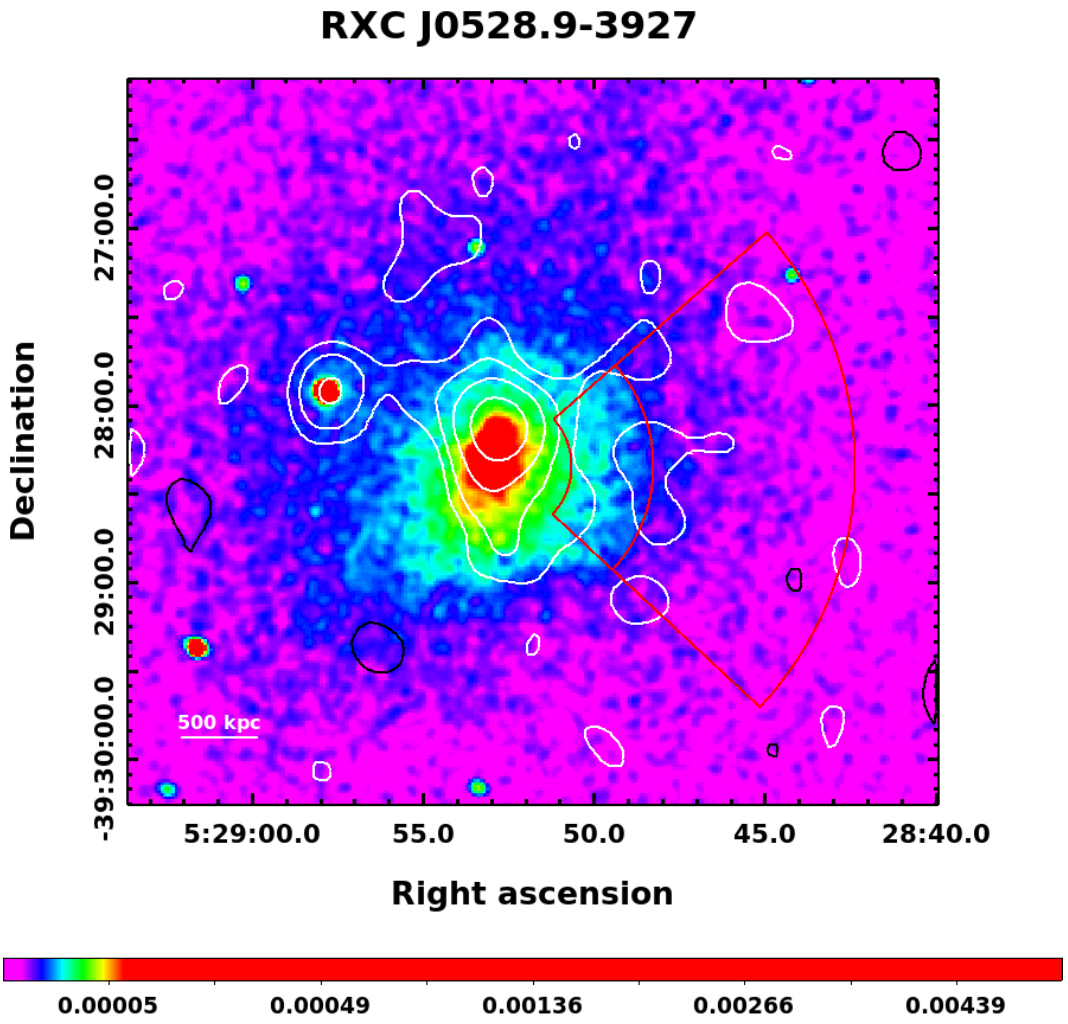

FIGURE 2.2: This is X-ray brightness map of the galaxy cluster RXC J0528.9-3927 (Botteon, Gastaldello & Brunetti, 2018) overlaid with radio contours . The colobar displays the temperature in keV.

using the image made with the full uv-range available. We reimaged the data to get the contribution of the point sources by restricting the uv-range to $> 4k\lambda$ to obtain the point source flux density ($F_\nu$pointsource). We finally imaged the data to get the extended emission (Flux density of extended source $F_\nu$extendedsource) by restricting the uv-range to $< 8k\lambda$.

We then look for the data at other frequencies for this galaxy cluster. We have found the images in the NRAO VLA Sky Survey (1.4 HZ, NVSS) (Condon et al., 1998), Sydney University Molonglo Sky Survey (810 MHz, SUMSS) (Mauch et al., 2003) and TIFR GMRT Sky Survey(150 MHz, TGSS) (Intema et al., 2017). At all the frequencies we are limited by the resolution i.e in these surveys the central

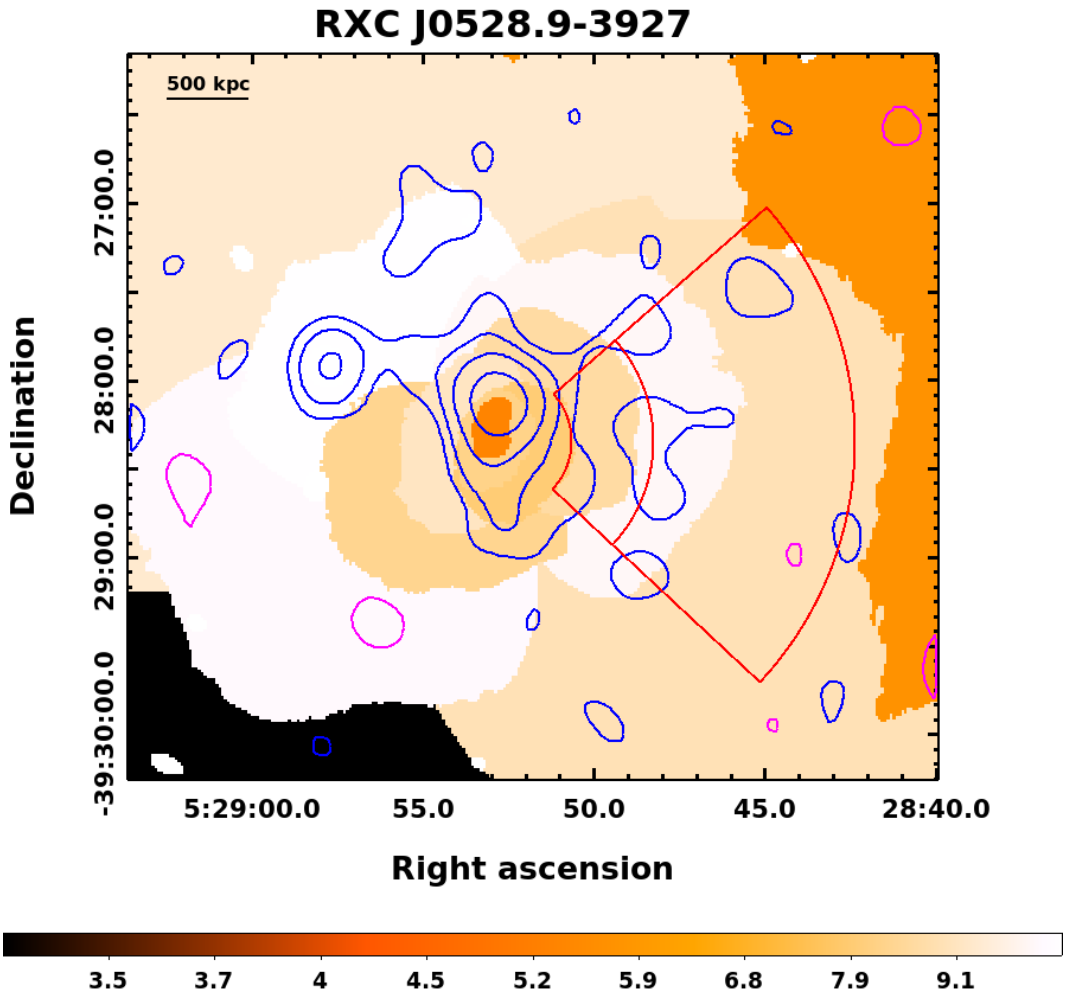

FIGURE 2.3: Temperature map for RXC J0528.9-3927 (Botteon, Gastaldello & Brunetti, 2018) overlaid with radio contours. An edge on the W is suggested temperature map after fitting the SB profile with broken power law gives us the $kT_u = 10.5^{+3.6}_{-1.8} keV$ and $kT_d = 10.5^{+0.9}_{-0.7} keV$ shows the presence of the cold front marked with in red color in figure. Color-scale has unit kT(keV).

point source and the extended emission are not resolved. Thus we calculate the flux density of the source as total flux density by fitting a Gaussian. We then use the following to obtain the flux density of the extended emission,

$$F_{\nu(\text{total})} = F_{\nu(\text{pointsource})} + F_{\nu(\text{extendedsource})}. \tag{2.1}$$

We assume a spectral index $\alpha = -0.75$ [1] for the central point source. Since we have point source flux density at 610MHz we then use the power law as follows:

[1]The spectral index, α is defined as $S_\nu \propto \nu^\alpha$, unless stated otherwise.

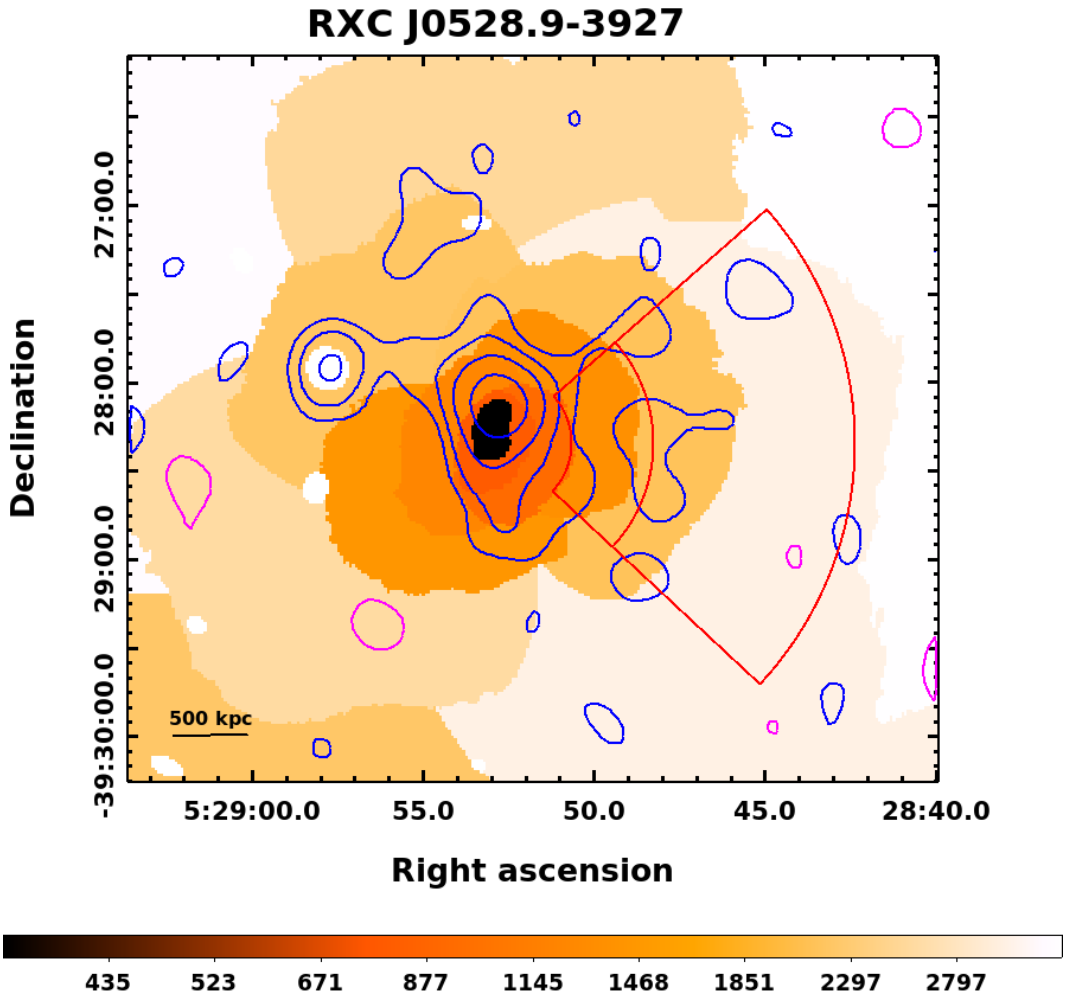

FIGURE 2.4: Figure shows the entropy map (Botteon, Gastaldello & Brunetti, 2018) overlaid with radio contours for the RXC J0528.9-3927 and X-ray emission peaked on the central low entropy region surrounded by hot gas.Color scale has unit K ($\mathrm{keVcm^{5/3}arcsec^{-2/3}}$) .

$F_\nu \propto \nu^{-\alpha}$, which gives us $\frac{F_{\nu_2}}{F_{\nu_1}} = (\frac{\nu_2}{\nu_1})^{-\alpha}$. Based on the assumptions that spectral index $\alpha = -0.75$ we got the point source flux density at other frequencies using the observed value of the point source flux density at 610 MHz. We then subtracted this value from the total source flux density to get the extended source flux density. We have summarised all the flux densities in the Table 2.2.

TABLE 2.2: For point source, extended source and total flux densities at different frequencies.

Frequency (MHz)	$F_{\nu(Total)}$**(mJy)**	$F_{\nu(\text{Pointsource})}$**(mJy)**	$F_{\nu(Extended)}$**(mJy)**
150	142±15	23±2	119±13
610	11±1	8±1	8±1
810	14±2	6±1	7±1
1400	6±1	4±0.5	2±0.2

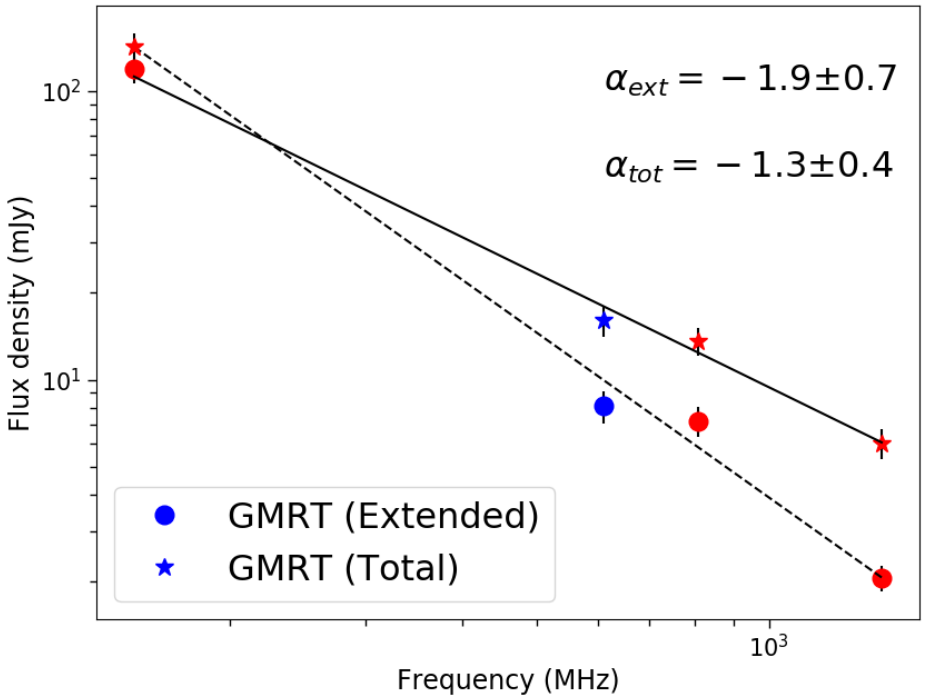

FIGURE 2.5: Blue star shows 610MHz GMRT data point.Blue filled circle shows total flux density at 610MHz and Blue filled star shows the extended source flux density at 610MHz.At other frequencies the filled red circle show flux density of extended source and filled red star shows the total flux density.

2.4.3 Calculation of the equipartition magnetic field

Clusterwide magnetic field is ubiquitous.The estimation of the cluster magnetic field is done with the assumption of the equipartition i.e filling factor is unity and energy density of magnetic field and cosmic rays is same.The value of the equipartition magnetic field typically varies from $0.1 - 1\mu$G (Carilli & Taylor, 2002, Ferrari et al., 2008, Govoni & Feretti, 2004a). The minimum energy density

U_{min} is given by,

$$U_{min} = \zeta(\nu_1, \nu_2, \alpha)(1+\kappa)^{4/7} \nu_{0(\mathrm{MHz})}^{4\alpha/7} (1+z)^{(12+4\alpha)/7} I_{0(\mathrm{mJy/arcsec^2})} d_{\mathrm{kpc}}^{-4/7} \tag{2.2}$$

where k is the ratio of energy in relativistic protons to that in electrons, α is the synchrotron spectral index, ν_0 is the frequency at which the surface brightness, I_0 is measured, d is the depth of the source and $\zeta(\alpha, \nu_1, \nu_2)$ is a parameter that is a function of the spectral index and the lower and higher limits in frequency, ν_1 and ν_2. The K-correction is included and a filling factor of 1 is assumed in the above equation. The magnetic field is then given by,

$$B_{eq(G)} = ((24\pi/7)U_{min})^{1/2} \tag{2.3}$$

We have found the following values of the parameters that required to calculate the cluster magnetic field.The depth of the cluster RXC J0528.9-3927 was taken as geometric mean of the maximum and minimum extent i.e (197.63 kpc $\times$ 376.13 kpc). The extent in the plane of sky over which the flux density of the RXC J0528.9-3927 was measured enclosed 759 beams with beam area of 100.2 arcsec^2 hence the surface brightness calculated to be 8.11mJy/(759 $\times$ 100.23arcsec^2). For $\alpha = 1.2$[2], $\nu_1 = 10$MHz, $\nu_2 = 10$GHz and central frequency ν_0 is 610MHz we found the $\zeta = 3.42 \times 10^{-13}$. The implied magnetic filed under these assumptions turns out to be 1.09μG.

2.4.4 Radio power of the diffuse emission

We have calculated the radio power using the luminosity distance, redshift and taking k correction into account.

$$P_{1.4GHz} = 4\pi F_\nu D_L^2 (1+z)^{-(\alpha+1)} \tag{2.4}$$

where the luminosity distance is $D_L = D_A(1+z)^2$, where D_A is angular distance and at z=0.284 for given cluster D_A is 911Mpc. Putting values of the $\alpha = 1.2$, D_L and $F_{1.4GHZ}$ (Table 2.2). We get the radio power for cluster RXC J0528.9-3927 $P_{1.4GHZ} = (6.06 \pm 0.7) \times 10^{25}$ W Hz^{-1}.

[2]the definition of spectral index in this formula is defined as $S_\nu \propto \nu^{-\alpha}$ (Govoni & Feretti, 2004b).

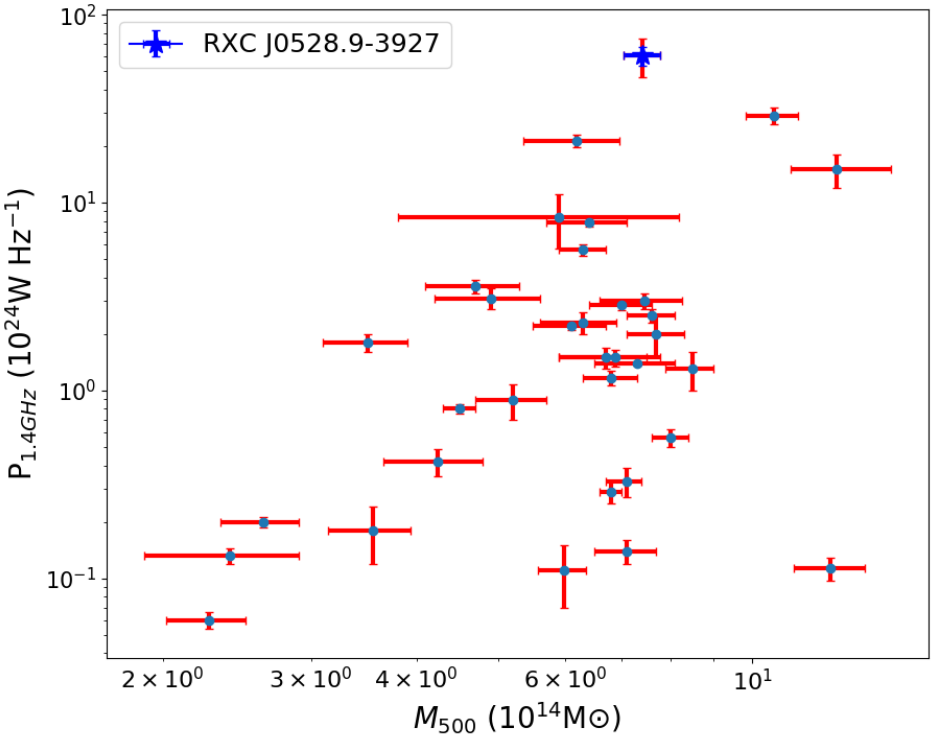

FIGURE 2.6: Radio power vs M_{500} for available sample of the mini halos.Blue star point indicates the RXC J0528.9-3927.

2.5 RXC J0528.9-3927: giant radio halo or mini-halo?

The classification of a diffuse source as a radio halo or a mini-halo is carried out based on the characteristics of the host cluster and that of the diffuse emission. It has been observed that the giant radio halos are mostly associated with the clusters which are undergoing merger phase (Cassano et al., 2010, Kale et al., 2015) and have sizes larger than 700 kpc. We calculated the average extent or radius of the diffuse emission as:

$$d_{minihalo} = \sqrt{d_{max} \times d_{min}} \tag{2.5}$$

where d_{max} and d_{mini} are the maximum and minimum extent of the diffuse emission derived from the $+6\sigma$ isocontours in the radio image (Cassano et al., 2007). This however depends on the signal to noise to of the images, so this gives us the lower limit for the real size. We found the size based under this assumptions is 272.6 kpc. This size is consistent with that of mini-halos rather than radio halos. The diffuse emission is also seen surrounding the central galaxy which is also typical of a mini-halo. The spectral index of the diffuse emission is found to be -1.9. However this is under our assumption of the BCG spectral index α to be -0.75.

Recently (Knowles et al., 2021) have reported this diffuse source as the radio halo with the radio power $\log(\mathrm{P_{1.4GHz}})$ to be $23.94^{-0.05}_{+0.06}$ with a largest linear size of the 0.54 Mpc. We have found the radio power $P_{1.4GHz}$ to be $6.7 \pm 0.7 \times 10^{25}$ $\mathrm{WHz^{-1}}$ and the largest linear size according to our result is 0.37 Mpc and it is smaller than the (Knowles et al., 2021).

Brunetti & Jones (2014b) have also suggested a scenario of whether mini halos can further evolve to become giant radio halos or do they have independent physical origins. This galaxy cluster hosts a cold front and the value of the central entropy which distinguish the cool core (CC) cluster from non cool cluster (NCC) for this cluster it is 73 ± 14 which indicates that this is a merging cluster. Thus this cluster has properties of a cool-core as well as a merging cluster and it contains a diffuse radio emission of size smaller than typical radio halos. Thus we term this as a mini-halo. However observations with better resolution at multiple frequencies are needed to fix spectral properties of diffuse radio emission and its extent in this galaxy cluster.

2.6 Summary and conclusions

- We have detected the presence of the radio diffuse emission in the galaxy cluster RXC J0528.9-3927 which extends up to 272.6 kpc. The X-ray brightness, temperature and the entropy maps together shows that diffuse radio emission is the consistent with the location the cold front.

- Since we were limited by only one observation at 610 MHz, we then assume the BCG spectral index of the $\alpha = -0.75$ and that total observed flux is contributed by two types of emission i.e point source flux density and extended source flux density. We then looked for the other surveys and found

the total flux density for this source from TGSS, NVSS and SUMSS. Based on the above assumption we have found the spectral index of the extended emission is $\alpha = -1.9 \pm 0.7$ and we placed this source as steep spectrum source. We then calculated the cluster magnetic field for the cluster and found it to be 1.09μG.

- We calculate the radio power for the RXC J0528.9-3927 and compare this with the existing sample of the mini halo radios by Richard-Laferrière et al. (2020) and it turns out to be the brightest. However our measurement is affected by the assumption of spectral index for the central radio source. Further observations with better resolution are needed to separately determine the properties of the central source and the extended emission.

- Finally the extent of the diffuse emission, its location surrounding the BCG and presence of the cold front in the cluster we come to conclusion that RXC J0528.9-27 is most likely a radio mini halo. However the central entropy indicates that this may be a merging cluster.

Chapter 3

Radio study of the galaxy cluster PLCKESZ G171.94-40.65

3.1 Introduction

PLCKESZ G171.94-40.65 cluster was discovered as part of the Planck Early Sunyaev–Zel'dovich (ESZ) all sky survey (Planck Collaboration et al., 2011b). The clusters in this survey are detected by noticing the distortion in the cosmic microwave background radiation (CMB) known as Sunyaev-Zel'dovich (SZ) effect (Sunyaev & Zeldovich, 1972). SZ effect is a powerful tool for detecting the massive clusters at high redshift. It is found that clusters detected in X-ray observations are biased towards cool core clusters (Rossetti et al., 2017). Cool core clusters follows a particular temperature profile i.e coldest region in the centre surrounded with hot plasma. While non cool core do not a single central peak due to the disturbance int he gas created by mergers. Since the Sunyaev–Zel'dovich effect measures the integrated pressure along the line of the sight using Compton y-parameter it can still detect the clusters which have gone through the recent mergers and do not have peaked X-rays at the centre.

PLCKESZ G171.94-40.65 was one of the newly discovered with the Planck satellite and has a mass of $1.5 \times 10^{15} M_{\odot}$ and redshift 0.27. It was later confirmed with XMM Newton X-ray observations. The general properties of the clusters are presented in Table 3.1.

TABLE 3.1: General properties of PLCKESZ G171.94-40.65. R.A and Dec. are coordinate of the X-ray peak, z is the iron K line, Luminosity , temperature KT Luminosity Lx and mass M_{500} corresponds to radius R_{500} (Giacintucci et al., 2013).

$R.A._{J2000}(hms)$	03 12 57.4
$Dec._{J2000}(dms)$	08 22 10
z_{Fe}	0.27
$L_{X[0.1-2.4]keV}(10^{45}ergs^{-1})$	1.13
$kT(keV)$	10.65
$M_{500}(M_{\odot})$	1.09×10^{15}
$D_L(Mpc)$	1364
Angular size(kpc/")	4.135

3.1.1 Discovery of giant radio halo in PLCKESZ G171.94-40.65

(Giacintucci et al., 2013) report the discovery of a giant radio halo in PLCKG171.9-40.7. The radio halo was found using the GMRT and the NRAO VLA Sky Survey images. They used the GMRT at 235 MHz and 610 MHz. They have speculated it as an ultra steep spectrum radio halo as they found the spectral index to be $\alpha = -1.84 \pm .14$ in the range 1.4 GHz to 235 MHz. The extent of the source was found to be 1364 kpc.

3.2 Radio data analysis

In order to study the properties of the radio halo in details, it deep observations with the GMRT and the JVLA were carried out (Table 3.2). GMRT data reduction are done with pipeline CAsa Pipeline-cum-Toolkitfor Upgraded GMRT data reduction - CAPTURE (Kale & Ishwara-Chandra, 2021). CAPTURE flags the bad data (bad channels, bad time span, bad antennas, radio frequency interference). After intial flagging it performs the calibration (fluxscale, delay, bandpass) and then finally performs imaging. Self-calibration with phase only and finally with amplitude and phase solutions worked out for six iterations. We have chosen the robust= 0 for imaging. Flux calibration is performed using standard flux scale of Perley-Butler 2017 (Perley & Butler, 2017). The visibilities after self-calibration were reimaged with a choice of lower limit on the uv-range to separate out the contribution of the point sources. We first created an image of point sources using

TABLE 3.2: Details of the observations are given here. Data at 235, 325 and 610 MHz are observed by GMRT and the data at 1400 MHz are observed with VLA in D array configuration. Corresponding bandwidths are written in column 3.

Observation Date	ν (MHz)	$\Delta\nu$ (MHz)	t_{tot} (hr)	restoring beam ",P.A(°)	rms (mJy beam^{-1})
2012 Dec29	235	32	5.5	12.35×10.0,78.85	0.44
2013 Jan5	325	32	5.5	9.07×7.42,84.06	0.11
2012 Dec29	610	32	5.5	5.04×4.20,76.70	0.05
2013 Mar17	1400	948	1.5	39.30×33.53,15.10	0.10

a lower cut off for the uv-range 4kλ and weighting scheme 'briggs'. The corresponding model was subtracted from the calibrated visibilities. We then created the final image with this visibility file using the uvrange $< 8k\lambda$. All the imaging is done with CASA task tclean and multi-frequency-synthesis (MFS) algorithm with two Taylor term (nterms= 1) to model the frequency dependence. We have used the gridder=wproject for widefield correction with wprojection planes= 256.

3.3 Halo Flux Density Calculator (HFDCA)

The popular method for calculation of the radio halo flux density is by finding the flux density within a region enclosing the $3-\sigma$ contours. However this method is very much dependent on the observations and the sensitivity. Basic idea behind this method are we draw the contours of the $3\sigma_{r.m.s}$ or $2\sigma_{r.m.s}$ where $\sigma_{r.m.s}$ is the root mean square noise. We calculate the flux density within these contours. This clearly suggests us that if we have deep observation this will definitely affect the measured value of the flux density i.e deep observation will increase the value of the flux density and poor observation will leads to decrements in the flux density.

Second popular method is due to (Murgia et al., 2009) where they first azimuthally average the surface brightness in concentric spherical annuli and after averaging fit the spherically symmetric exponential model to one dimensional radial surface brightness profile of the from

$$I(r) = I_0 e^{-r/r_e}, \tag{3.1}$$

where r_e is the characteristic e-folding distance from the halo centre and I_0 is the central brightness. But the main advantage of this method of fitting exponential

form is that now flux density value does not dependent on the depth of the observations. This method was extensively used to calculate the flux density for radio halos but the method has its limitations. These lie in the ideal circular distribution assumptions. There are radio halos which follow elongated morphology and many of them are asymmetric (e. g. Feretti et al., 2012).

The idea behind the Halo Flux Density calculator (Halo-FDCA) is to generalise the above fitting method for more variety of the radio halos by invoking the different models i.e not restricting oneself to circular model only. Boxelaar, van Weeren & Botteon (2021) generalised this circular model by introducing a function $G(r)$ as follows:

$$I(r) = I_0 e^{-G(r)}. \tag{3.2}$$

In case of the circular model $G(r)$ reduced to $|r|/r_e$ and coordinate offset will be taken into account by replacing the $|r|$ by $|r - r_0|$ with these it becomes four parameter model $[I_0, x_0, y_0, r_e]$. They further increase the parameter space up to six by making model applicable for the elliptical distribution and finally they include the most generalised case of the skewed model with off-center maximum makes parameter number up to eight. To fit the flux density profile Boxelaar, van Weeren & Botteon (2021) have used the Markov Chain Monte Carlo (MCMC) simulation which is based on the the Bayesian inference. In this case it finds the model parameters that maximize the likelihood function. We apply this method in the study of this cluster.

3.4 Results

We have imaged the radio data using an automated pipeline CAPTURE (Kale & Ishwara-Chandra, 2021) and come up with the robust 0 images at frequencies 235 MHz, 325 MHz and 610 MHz. We then used CASA task uvsub and subtracted the point sources from the data set and reimaged the data which gave us purely extended emission, which we have described below. We then calculate the integrated spectrum for the radio halo and also calculated the cluster magnetic field. We also list the discrete radio sources around the centre.

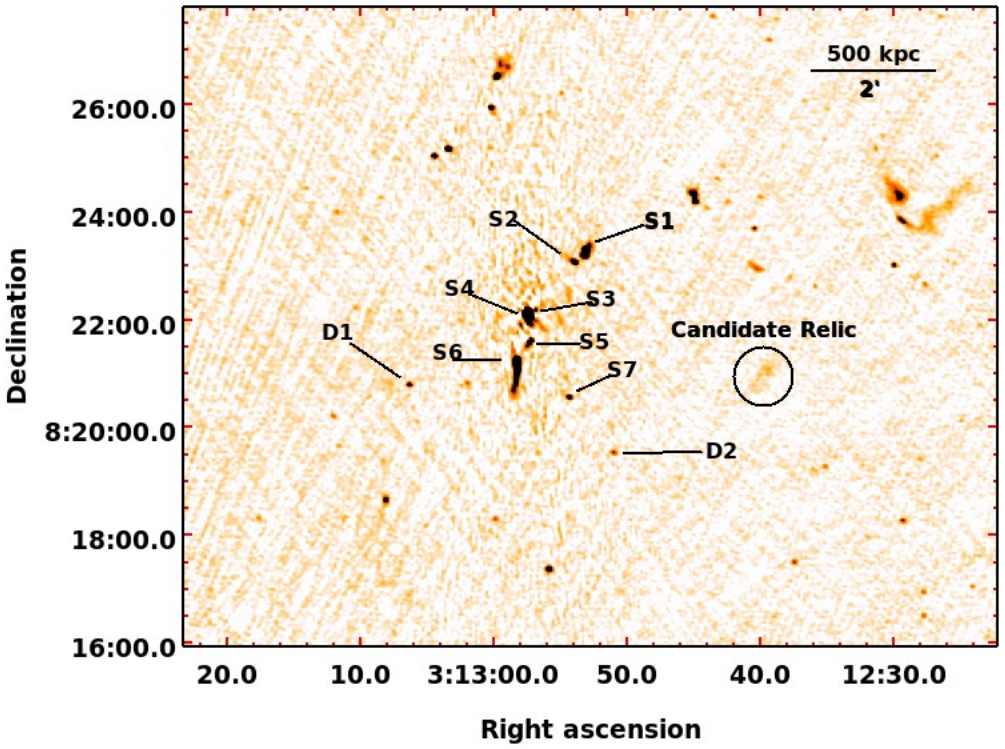

FIGURE 3.1: This is the image of PLCKESZ G171.94-40.65 at 610 MHz with marked sources within the region of 2.5 Mpc radius. The restoring beam is 5.04"×4.20".

3.4.1 Radio robust 0 images

We present the Fig. 3.1, where the high resolution 610 MHz image with discrete source marked in the region. We have presented the 235 MHz image in Fig. 3.2. The restoring beam is 12.35"×10.0" in P.A 78.8°. The positive blue contour levels are 6σ,12σ,24σ and negative contours are shown with green colour at -4σ. The σ is 0.44mJy beam^{-1}. In Fig. 3.3 we have shown 325 MHz image with a restoring beam 9.07"×7.42" and P.A 84.06°. Positive blue contours levels are 6σ,12σ,24σ and negative green contours are -3σ, where σ is 0.11 mJy beam^{-1}. The candidate relic is marked with circle in the image. In Fig. 3.4 we have shown GMRT 610 MHz image is in colour and contours. The restoring beam is 5.04"×4.20" in P.A 76.70°. Positive contour levels are 3σ, 6σ,12σ,24σ where σ is 0.050 mJy beam^{-1} and shown in blue while negative contours shown with green colour are at -4σ. In Fig. 3.5 we have shown 1400MHz (VLA-L band image observed with D array configuration) image of restoring beam 39.30"×33.53" and P.A 15.1°. The positive blue contour levels are 6σ,12σ,24σ,48σ and negative green contour corresponds to 3σ, where σ is 0.10 mJy beam^{-1}.

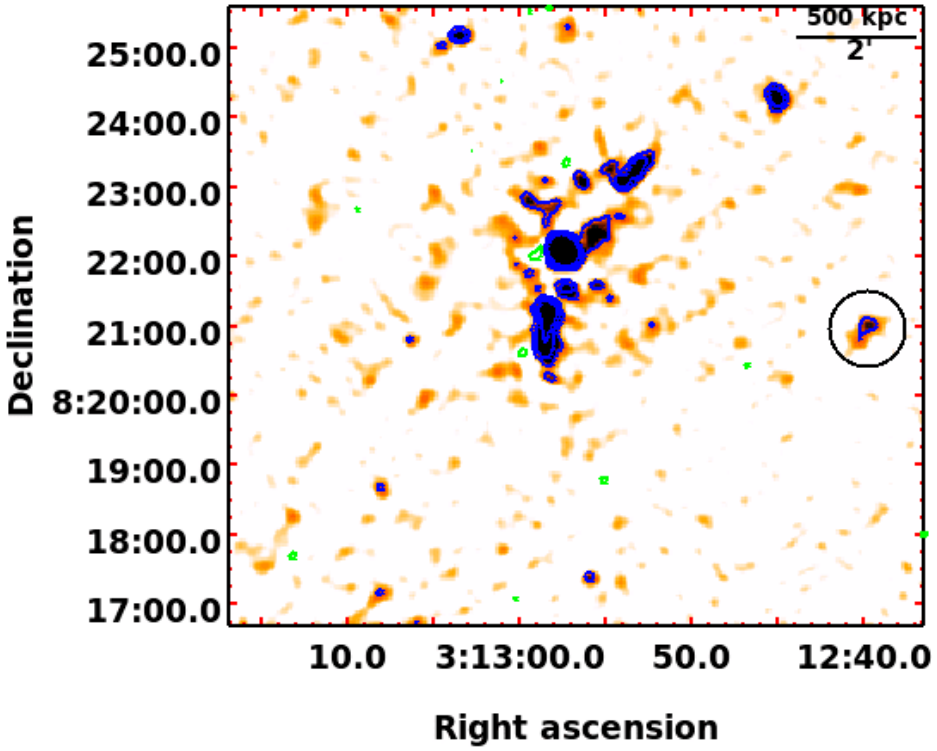

FIGURE 3.2: We have shown the image at 235 MHz with restoring beam 12.35"×10.0" and P.A 78.8°. The positive blue contour levels are 6σ,12σ,24σ and negative contour shown with green colour is -4σ, σ is 0.44mJy beam^{-1}.

3.4.2 Discrete radio sources near the cluster centre

In the Table. 3.3 we have noted the positions of the discrete sources in the field of view. The sources S_1 to S_7 are as same as in Giacintucci et al. (2013). We have noted three new discrete sources named as D_1, candidate relic and D_2. The morphologies of the sources S_1 to S_7 are given in the (Giacintucci et al., 2013), however we have updated the flux density and spectral index according to our observed value. We have marked these sources in the Fig. 3.1. D_1 and D_2 have the unresolved morphology and the candidate relic is an extended structure. The corresponding values of the spectral index for these sources are shown in the Table. 3.3. We have a separate subsection for the candidate relic, Section. 3.5.

3.4.3 Extended Emission Images

We have shown the point source subtracted images in this section made using the script mentioned in the previous chapter (Sec. 2.3). We have shown the positive

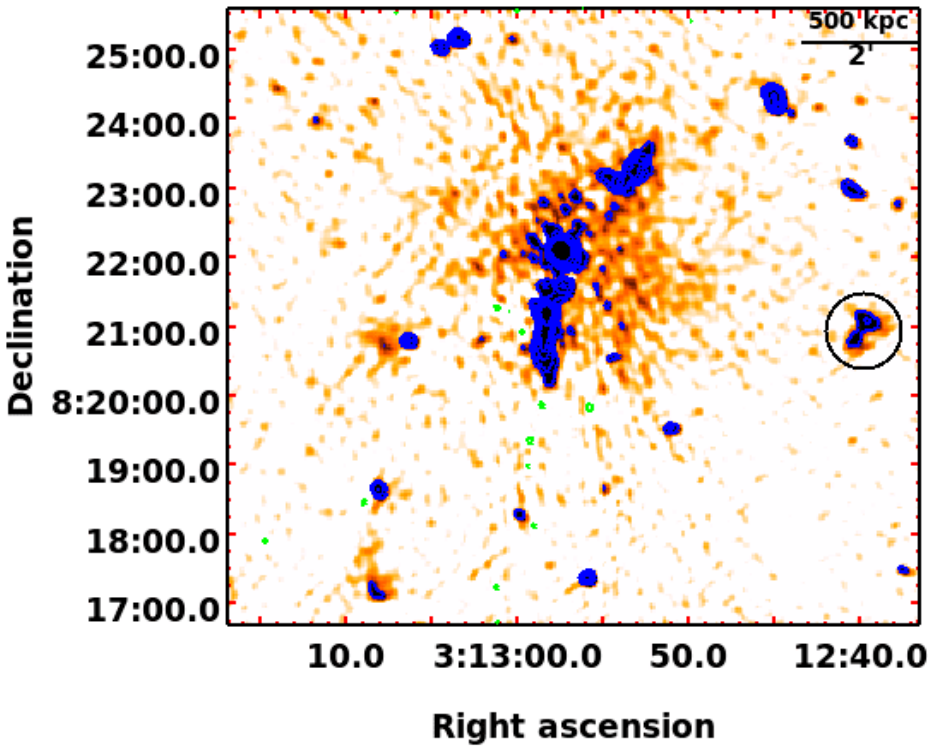

FIGURE 3.3: The 325 MHz image with a restoring beam 9.07"×7.42" with P.A 84.06° is shown. Positive blue contours levels are 6σ,12σ,24σ and negative green contour is -3σ, where σ is 0.11 mJy beam^{-1}.

TABLE 3.3: Discrete radio sources in PLCKESZ G171.94-40.65 and the candidate relic (CR).

Source	RA$_{J2000}$ hh mm ss	DEC$_{J2000}$ ° ′ ″	S_{235MHz} (mJy)	S_{325MHz} (mJy)	S_{610MHz} (mJy)	Spectral Index
S1	03 12 53.2	+08 23 12	-	17 ± 2	13 ± 1	-0.4 ± 0.2
S2	03 12 53.9	+08 23 05	-	8 ± 1	6 ± 1	-0.5 ± 0.2
S3	03 12 56.9	+08 22 11	-	-	2 ± 0.2	-
S4	03 12 57.5	+08 22 09	-	-	195 ± 22	-
S5	03 12 57.3	+08 21 37	-	7 ± 1	5 ± 1	-0.4 ± 0.2
S6	03 12 58.3	+08 21 14	-	71 ± 7	47 ± 5	-1 ± 0.2
S7	03 12 54.4	+08 20 35	-	6 ± 1	3 ± 0.3	-1.3 ± 0.2
D1	03 13 06.3	+08 20 48	-	4 ± 0.4	2 ± 0.3	$-1 \pm .2$
CR	03 12 39.6	+08 21 02	12 ± 1	8 ± 1	-	-1.1 ± 0.4
D2	03 12 50.9	+08 19 32	-	2 ± 0.2	1 ± 0.2	-1 ± 0.3

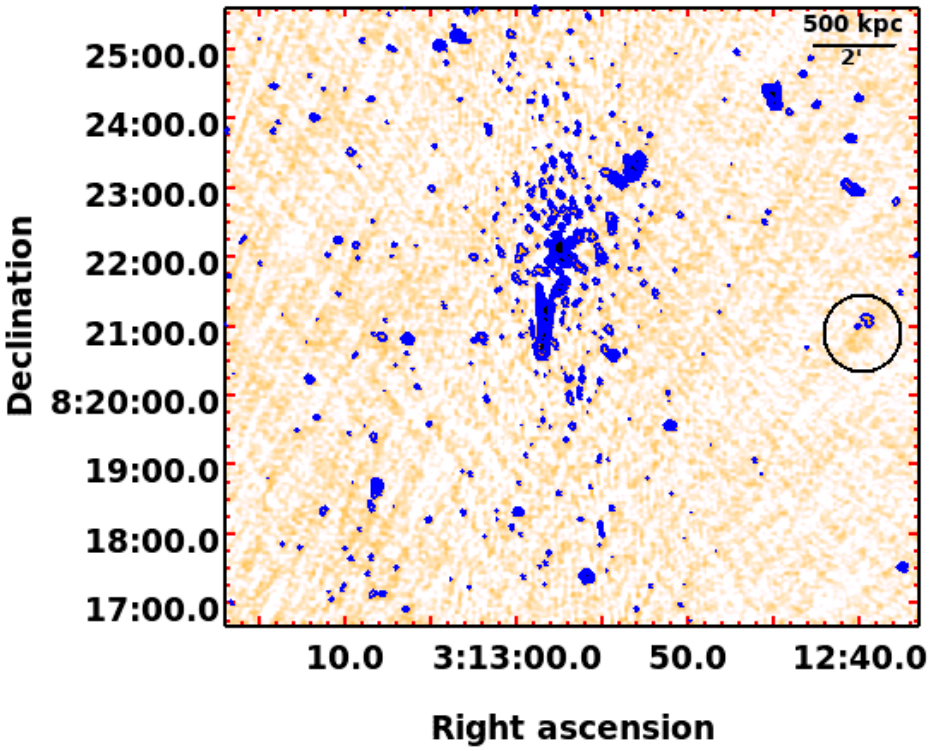

FIGURE 3.4: GMRT 610 MHz image is shown in colour and contours. The restoring beam is 5.04"×4.20" with P.A 76.70°. Positive contour levels are 3σ, 6σ,12σ,24σ where σ is 0.050 mJy beam^{-1} and shown in blue While negative contour shown with green colour is at -4σ.

contours in black and negative in magenta colour. We have detected the extended emission at 325 MHz (Fig. ??) and at 1400 MHz (Fig. 3.7). We have also shown 1400 MHz radio contours overlaid with X-ray brightness map (Fig. 3.8). The 1400 MHz image overlaid on the X-ray emission was made without the inner uv-range cut. The Fig. 3.7 is produced with uv-range matched with that of the 325 MHz image.

3.4.4 Integrated spectrum of the radio halo

We have chosen the circular model while running the Halo FDCA pipeline to model the radio halo. Table. 3.4 shows the best fitted parameters and the value of the flux density based on the Halo FDCA method. We have plotted the integrated spectrum taking the values of flux density at different frequencies Fig. 3.9 . We have used the Halo-FDCA flux outcome to plot the integrated spectrum. At 235

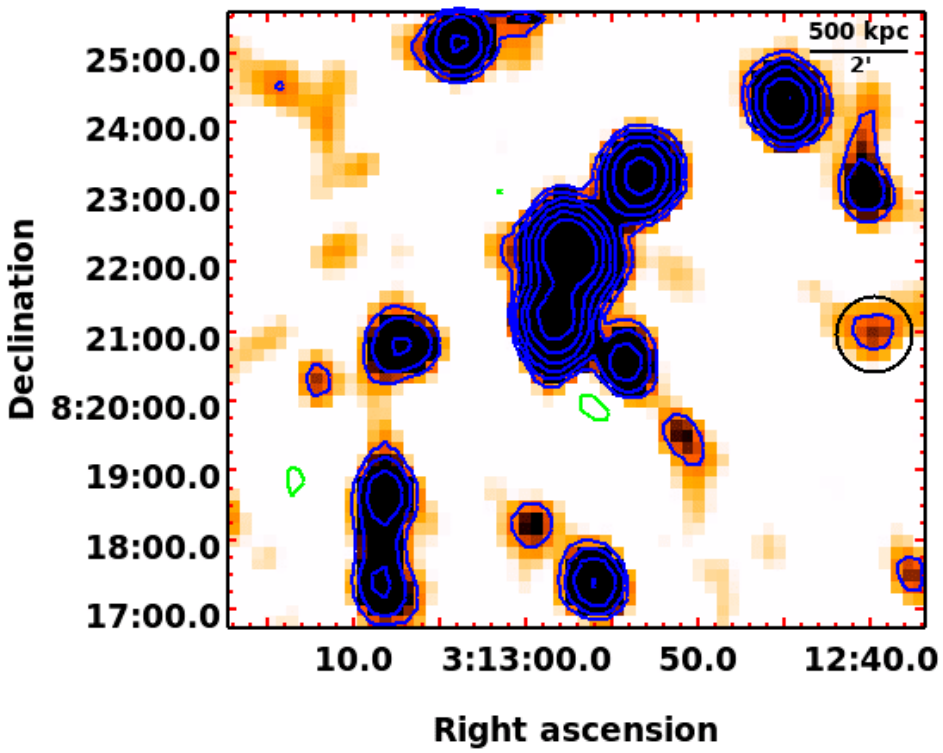

FIGURE 3.5: We have shown 1400 MHz (VLA-L band image observed with D array configuration) image with a restoring beam 39.30"×33.53" and P.A 15.1°. The positive blue contour levels are 6σ, 12σ, 24σ,48σ and negative green contour is corresponds to 3σ, where σ is 0.10 mJy beam^{-1}. In all the above images we have marked a circular region which indicates the candidate relic.

MHz, 325 MHz and 610 MHz we had GMRT observations and at 1400 MHz we used the JVLA observation for the galaxy cluster.

3.4.5 Halo Flux density Calculator (HFDCA) Comparison with the CASA flux density values

Table. 3.4 shows the best fitted parameters and the value of the flux density based on the Halo FDCA method. We have chosen the circular model while running the Halo FDCA pipeline. Here in this section we would like to compare the radio flux densities densities from Halo-FDCA and traditional CASA region method where we just calculate the flux enclosed within the $3\sigma_{r.m.s}$ or any other value depending upon the depth of the observation. We have shown the Fig. 3.10 for the corner plot for at GMRT-325 MHz and VLA-1400 MHz. Plots are showing the maximization of the likelihood function and also shows the parameters space distribution.

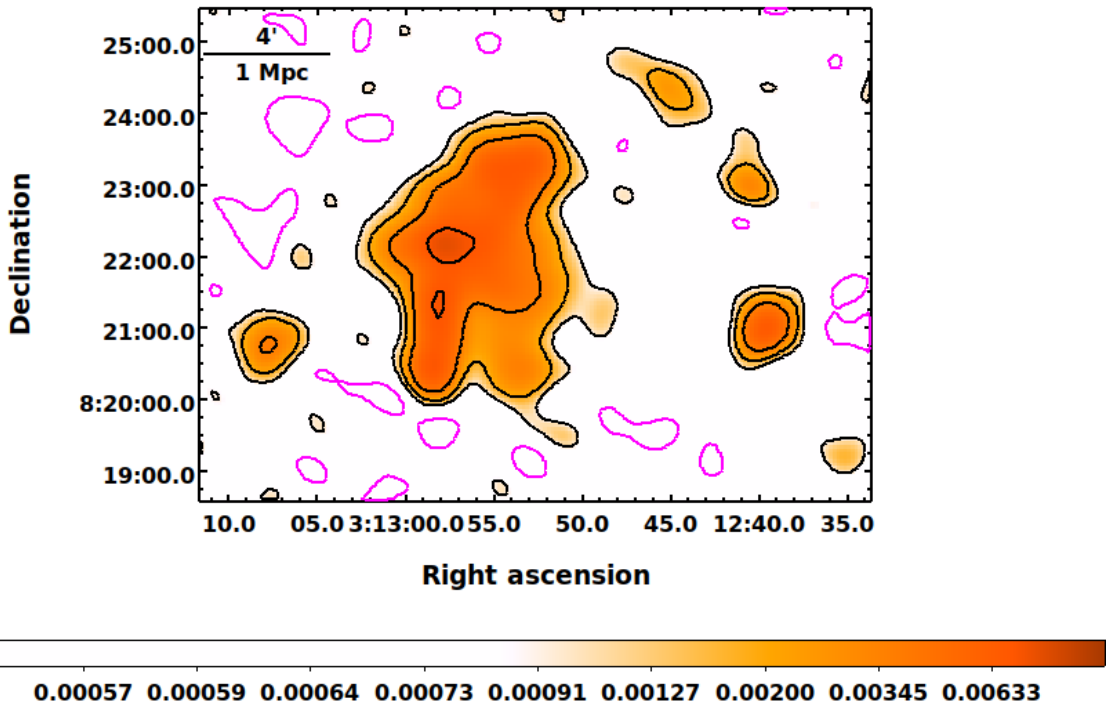

FIGURE 3.6: The 325 MHz image of the extended emission. The restoring beam is 35"×35" and the $\sigma = 0.8$ mJy/beam. The positive contours at 3σ, 6σ and 12σ are shown in black. Negative contours are shown in magenta colour corresponding to -3σ.

TABLE 3.4: Details of the fitted parameters and outcome from Halo-Flux density calculator

ν (MHz)	$I_\circ$ μJy/arcsec^2	$x_\circ$ (deg)	$y_\circ$ (deg)	r_e (kpc)	χ^2	F_ν mJy
325	15	48.23	8.36	176	0.74	171±8
1400	1	48.21	8.39	305.83	0.87	35±1.5

We have seen that the characteristic e fold distance turn out to be higher at 1400 MHz (305 kpc) and at 325 MHz it is 176 kpc it may be due of the flattening of the spectral index or may be due to the specific nature of the radio halo in the galaxy cluster. Since the highest resolution available for point source subtraction is different at the two frequencies, the amount of contamination due to residuals from discrete sources is likely to be higher at 1400 MHz. This may also have resulted in a larger e-folding radius for 1400 MHz.

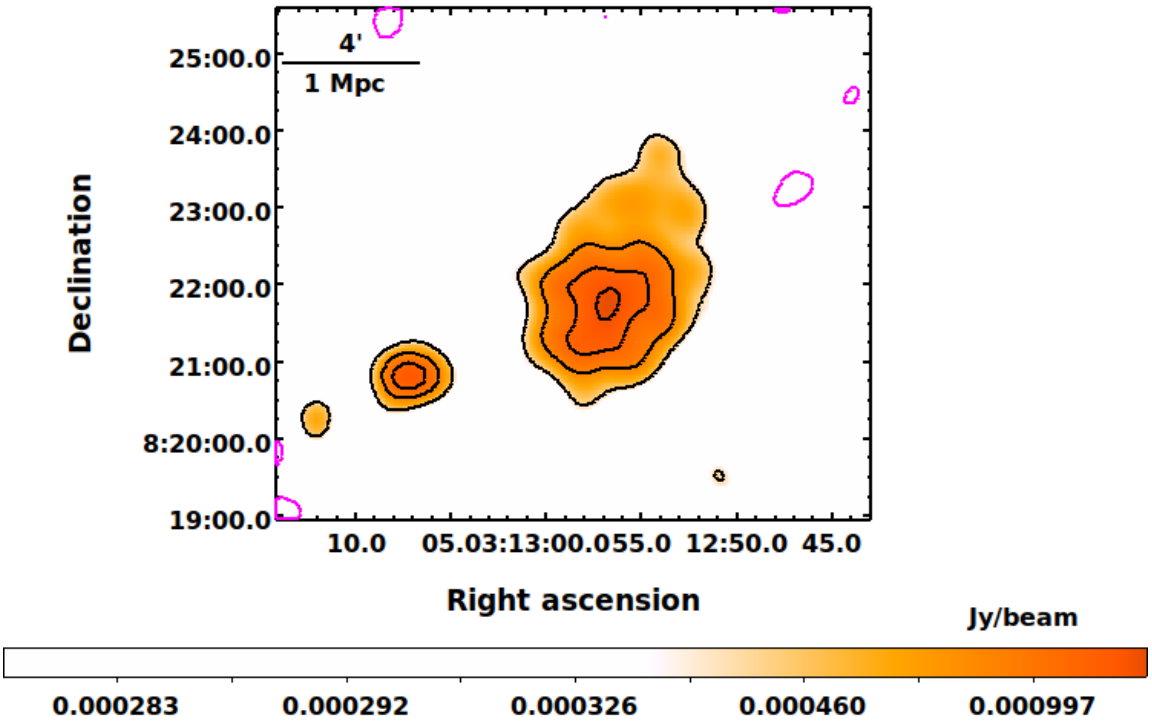

FIGURE 3.7: We have shown the 1400 MHz image of the extended emission with a restoring beam 35"×35" with $\sigma = 0.6$mJy/beam. The positive contours at 3σ, 6σ and 12σ are shown in black. Negative contours are shown in magenta colour corresponding to -3σ.

TABLE 3.5: Comparison of flux densities in Halo-FDCA and CASA within 3σ contours.

ν (MHz)	$F_\nu CASA$ mJy	F_νFDCA mJy
235	266±29	NA
325	162±20	171±8
1400	26±4	35±2

3.4.6 Calculation of the equipartition magnetic field

Cluster-wide magnetic field is ubiquitous (e. g. Carilli & Taylor, 2002). The estimation of the cluster magnetic field is done with the assumption of the equipartition i.e filling factor is unity and energy density of magnetic field and cosmic rays is same. The value of the equipartition magnetic field typically varies from $0.1 - 1\mu G$ (Carilli & Taylor, 2002, Ferrari et al., 2008, Govoni & Feretti, 2004a).

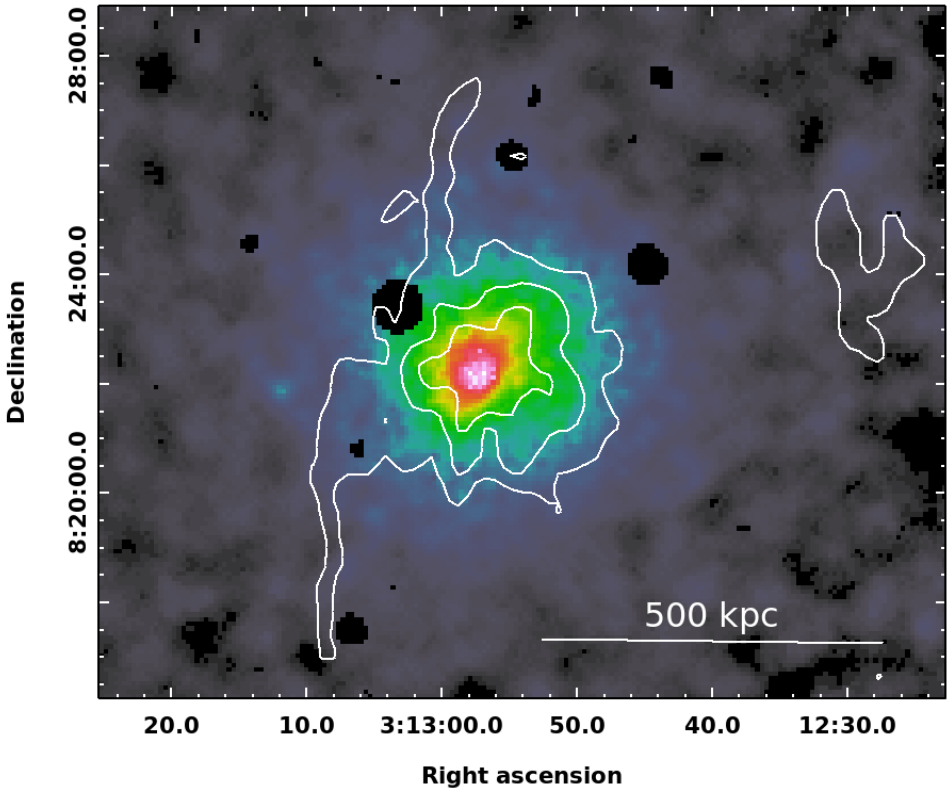

FIGURE 3.8: This is diffuse X-ray image of PLCKESZ G171.94-40.65 overlaid with the radio contours with $\sigma = 0.04$ mJy/beam and positive contours 3σ, 6σ and 12σ shown in white colour.

The minimum energy density U_{min} is given by,

$$U_{min} = \zeta(\nu_1, \nu_2, \alpha)(1+\kappa)^{4/7}\nu_{0(MHz)}^{4\alpha/7}(1+z)^{(12+4\alpha)/7}I_{0(mJy/arcsec^2)}d_{kpc}^{-4/7} \tag{3.3}$$

where k is the ratio of energy in relativistic protons to that in electrons, α is the synchrotron spectral index, ν_0 is the frequency at which the surface brightness in this case we chose it 1400 MHz, I_0 is measured, d is the depth of the source and $\zeta(\alpha, \nu_1, \nu_2)$ is a parameter that is a function of the spectral index and the lower and higher limits in frequency, ν_1 and ν_2. The k-correction is included and a filling factor of 1 is assumed in the above equation. The magnetic field is then given by,

$$B_{eq(G)} = ((24\pi/7)U_{min})^{1/2} \tag{3.4}$$

We have found the following values of the parameters that are required to calculate the cluster magnetic field. The depth of the cluster PLCKESZ G171.94-40.65 was

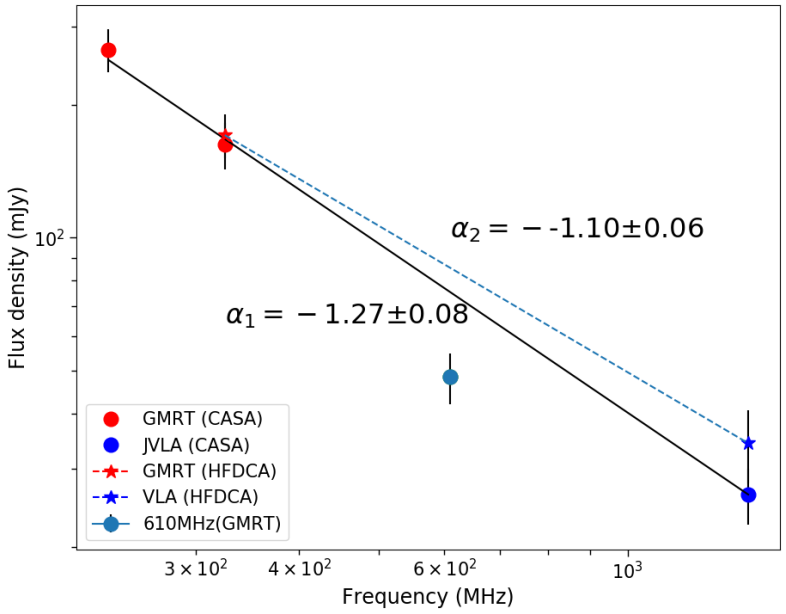

FIGURE 3.9: We have shown the integrated spectra for radio halo in the PLCKESZ G171.94-40.65. We have used the GMRT 235MHz, 325 MHz and VLA 1400 MHz to plot integrated spectrum (where flux densities were measured using CASA taking region of the 3σ contours). We got the value of the spectral index $\alpha_1 = -1.27 \pm 0.08$ and we have used the GMRT 325 MHz and VLA 1400MHz to get the integrated spectrum (where flux densities are calculated using the Halo Flux Density Calculator). We have got the spectral index to be $\alpha_2 = -1.10 \pm 0.04$.

taken as geometric mean of the maximum and minimum extent i.e (1.089 Mpc $\times$ 1.296 Mpc). The extent in the plane of sky over which the flux density of the PLCKESZ G171.94-40.65 was measured as enclosed 356 beams with beam area of 16.71 arcsec^2 hence the surface brightness was calculated to be 19.72mJy/(356 $\times$ 16.71$arcsec^2$). For $\alpha = 1.27$[1], $\nu 1 = 10$ MHz, $\nu_2 = 10$ GHz and central frequency ν_0 is 1400 MHz we found the $\zeta = 1.89 \times 10^{-13}$. The implied magnetic field under these assumptions turns out to be 3.43μG.

[1]the definition of spectral index in this formula is defined as $S_\nu \propto \nu^{-\alpha}$ (Govoni & Feretti, 2004b).

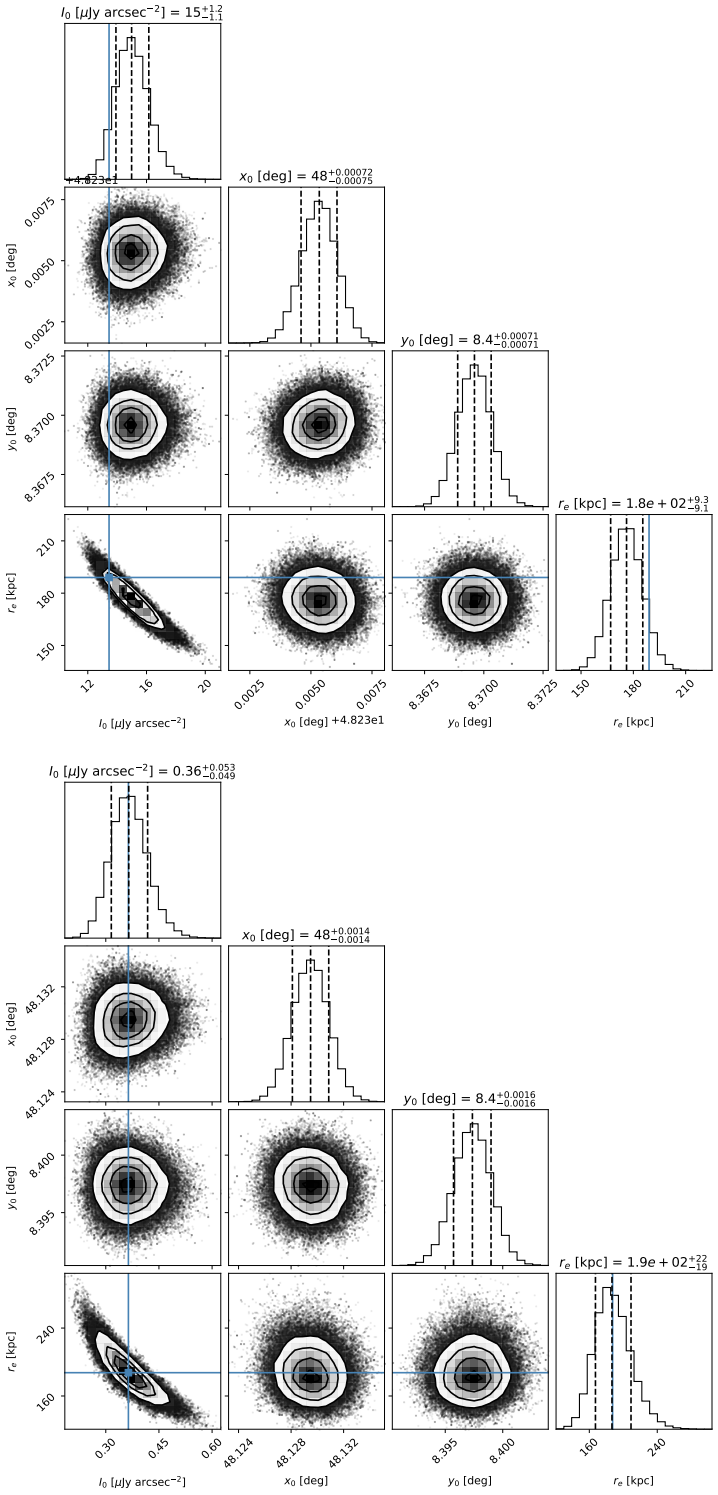

FIGURE 3.10: The above figures show the corner plots of the MCMC which are corresponding to maximization of the likelihood function. At the top we show the corner plot for 325 MHz and at the bottom we show the corner plot for 1400 MHz.

3.5 A suspected radio relic in PLCKESZ G171.94-40.65

We have detected a diffuse structure on the cluster periphery whose dimensions are maximum length 66" and maximum width of 41" at 235 MHz (or maximum length 74.5 kpc and maximum width 45.6 kpc) and same structure is also detected at 325 MHz and 610 MHz. We have marked Fig. 3.2, Fig. 3.3 and Fig. 3.4 with black colored circle in each radio robust zero image to show this diffuse structure. As cluster PLCKESZ G171.94-40.65 (Giacintucci et al., 2013) already hosts a giant radio halo which indicates that the strong merger of two sub cluster has occurred due to which the giant radio halo formed. However there are classes of the galaxy clusters which host both radio halo and radio relics (e. g. A2744, A2256). Radio relics are an indicator of the shock waves that accelerate the cosmic ray electrons in the direction of the motion of the shock waves and leads to formation of the large arc-like structures in the cluster periphery. We have calculated the spectral index for this suspected source taking the total flux. Its spectral index turns out to be -1.07 ± 0.43.

3.6 Discussion

We have the detected the radio halo emission in deep GMRT observation at 235 MHz, 325 MHz and 610 MHz and at 1400 MHz in the VLA-D array observation. We confirmed the presence of the radio emission at each of the each of the frequency. Earlier study on this cluster reported the integrated spectral index of the radio halo to be -1.84 ± 0.14 (Giacintucci et al., 2013). We have found the integrated spectral index value of -1.25 ± 0.31. Thus we find it to be a radio halo with a typical spectral index. We have adopted the method of the Halo flux density calculator to calculate the flux density. However this does not effect the value of the integrated spectral index as we have compared the CASA flux density value and the values resulting from HALO-FDCA (Table. 3.5). The Halo-FDCA values are found to be greater than the CASA values. The reason for this may be that the e-folding distance is beyond the region enclosed by CASA region.

We have detected the a diffuse radio source which may be a candidate relic as it is located at boundary of the cluster. We need deeper observation for the

confirmation of the relic. In Table. 3.3 we have shown this candidate relic and found the and the extent of this source 74.5 kpc × 45.6 kpc. Deep observation may help us to resolve the source as we might getting the the flux only due to brightest portion of this source. X-ray observation may help us to confirm the presence of the shock in this region of the cluster. The spectral index is about -1.0 which is not very steep. Thus due to absence of a radio core in our observations and the small extent, this can be a radio phoenix. Better sensitivity may be useful for us to decide the nature of this source right now the extent and spectral index do not provide sufficient evidence.

3.7 Summary and conclusions

- We have detected the presence of the diffuse radio halo emission in the galaxy cluster PLCKESZ G171.94-40.65 at all the frequencies 235 MHz, 325 MHz, 610 MHz and 1400MHz . We have shown the radio images, and those overlaid with X-ray surface brightness map.
- Discrete radio source and their properties are summarised in Table. 3.1.
- We have calculated integrated spectral index and magnetic field and radio power for the galaxy cluster PLCKESZ G171.94-40.65.
- We have discussed the new method Halo-FDCA for calculating the flux density of radio halos and compared its values of the flux density with CASA flux density values (Table. 3.5). The spectral index of the radio halo that we found does not place it in the ultra-steep spectrum radio halo category.
- We also found the suspected relic in the periphery of the cluster with extent of the 74.5 kpc×45.6 kpc. With these observations we cannot decide the nature of this source named it as a candidate relic as extent and spectral index do not help us decide the class of this source.

Chapter 4

A statistical study of radio halos

4.1 Introduction

In the growing number of the large cluster scale diffuse radio sources (van Weeren et al., 2019a) it could be useful to investigate the statistical behaviour of the these sources. It has been observed that some radio halos show ultra steep spectra i.e the value of the spectral index is a large negative number, > -1.5[1]. These may be radio halos hosted in less massive clusters or in clusters where the mergers have not been efficient in efficiently powering turbulence for particle acceleration. A statistical study may be a useful tool to relate the cluster mass with the radio power and spectral indices we observe, as dissipation of gravitational potential energy can be the main source for the energy powering the radio halos.

If massive clusters are involved in more energetic mergers and thus have more turbulence, then the radio halos in those clusters may have flatter spectral indices, assuming that the efficiency of particle acceleration is not affected by other factors. The inverse Compton energy losses increase with redshift and thus radio halos are likely to become steeper at higher redshifts. In this chapter we specifically analyse the trends between spectral indices of radio halos, host cluster masses and redshifts. We also show the location of the cluster PLCKESZ G171.94-40.65, studied in Chapter 3 in relation to the rest of the sample of radio halos.

[1]In this chapter we follow the convention: $S_\nu \propto \nu^\alpha$, where S_ν is the flux density at frequency ν and α is the spectral index.

4.2 Sample of the radio halos

The sample of all the diffuse radio sources in clusters known then was presented by van Weeren et al. (2019b) on the website `www.galaxyclusters.com`. We have updated the sample with the discoveries reported after that and presented those in the Table 4.1. We have a total of 89 radio halos.

For the analysis here, we have chosen the galaxy clusters that host a radio halo and are observed at more than one frequency. We have a sub-sample of 33 radio halos.

TABLE 4.1: The Columns of the table are [1]-Name of the cluster, [2]-R.A (Deg), [3]-DEC. (Deg), [4]-redshift, [5]-Mass($10^{15} M_{\odot}$), [6]-Positive error in mass ($10^{14} M_{\odot}$), [7]-Negative error in mass ($10^{14} M_{\odot}$), [8]-Flux density (Jy), [9]-Error in flux desnity,[10]-Reference, [11]-Frequency of the observation, [12]-Class, [13]Largest Angular Size (Mpc) References: (a) (Xie et al., 2020), (b) (Hoeft et al., 2020), (c) (Di Gennaro et al., 2021), (Raja et al., 2020), (Kale, Shende & Parekh, 2019)

[1]	[2]	[3]	[4]	[5]	[6]	[7]	[8]	[9]	[10]	[11]	[12]	[13]
Abell S1063	342.182	-44.52	0.346	1.14	0.03	0.03	0.0243	0.0025	(a)	325	halo	-
Abell S1063	342.182	-44.52	0.346	1.14	0.03	0.03	0.0058	0.0004	(a)	1500	halo	-
Abell S1063	342.182	-44.52	0.346	1.14	0.03	0.03	0.0017	0.0002	(a)	3000	halo	-
Abell 370	39.966	-1.58	0.375	0.76	0.06	0.06	0.02	0.0023	(a)	325	halo	-
Abell 370	39.966	-1.58	0.375	0.76	0.06	0.06	0.0037	0.0003	(a)	1500	halo	-
Abell 370	39.966	-1.58	0.375	0.76	0.06	0.06	0.0013	-	(a)	3000	halo	-
Abell 1430-A	179.82	49.79	0.35	0.76	0.04	0.04	0.021	0.006	(b)	144	halo	-
Abell 1430-A	179.82	49.79	0.35	0.76	0.04	0.04	0.0011	0.00015	(b)	1500 -	halo	-
PSZ2G086.93+53.18	228.47	52.79	0.67	0.54	-	-	0.0072	0.0015	(c)	144	halo	0.5
PSZ2G089.39+69.36	208	43.48	0.68	0.57	-	-	0.0125	0.0019	(c)	144	halo	1.0
PSZ2G091.83+26.11	277.78	42.248	0.82	0.74	-	-	0.0843	0.0127	(c)	144	halo	1.2
PSZ2G091.83+26.11	277.78	42.248	0.82	0.74	-	-	0.25943	0.0389	(c)	144	relic	1.2
PSZ2G099.86+58.45	213.70	54.77	0.61	0.68	-	-	0.0278	0.004	(c)	144	halo	1.2
PSZ2G126.28+65.62	190.64	51.44	0.82	0.5	-	-	0.0088	0.0.0017	(c)	144	halo	0.8
PSZ2G141.77+14.19	70.27	68.22	0.83	0.77	-	-	0.0088	0.0014	(c)	144	halo	0.6
PLCKG147.3–16.6	164.39	58.01	0.645	0.65	-	-	0.0225	0.0037	(c)	144	halo	0.8
PSZ2G160.83+81.66	186.74	33.54	0.88	0.57	-	-	0.013	0.002	(c)	144	halo	0.7
SPT-CL J20314037	307.96	-40.6	0.34	0.98	0.015	0.015	0.0169	0.00176	(d)	325	halo	-
SPT-CL J20314037	307.96	-40.6	0.34	0.98	0.015	0.015	0.0014	0.00018	(d)	1700	halo	-
RXCJ0232.2-4420	38.07	-44.3	0.28	1.2	0.18	0.18	0.052	0.005	(e)	606	halo	-

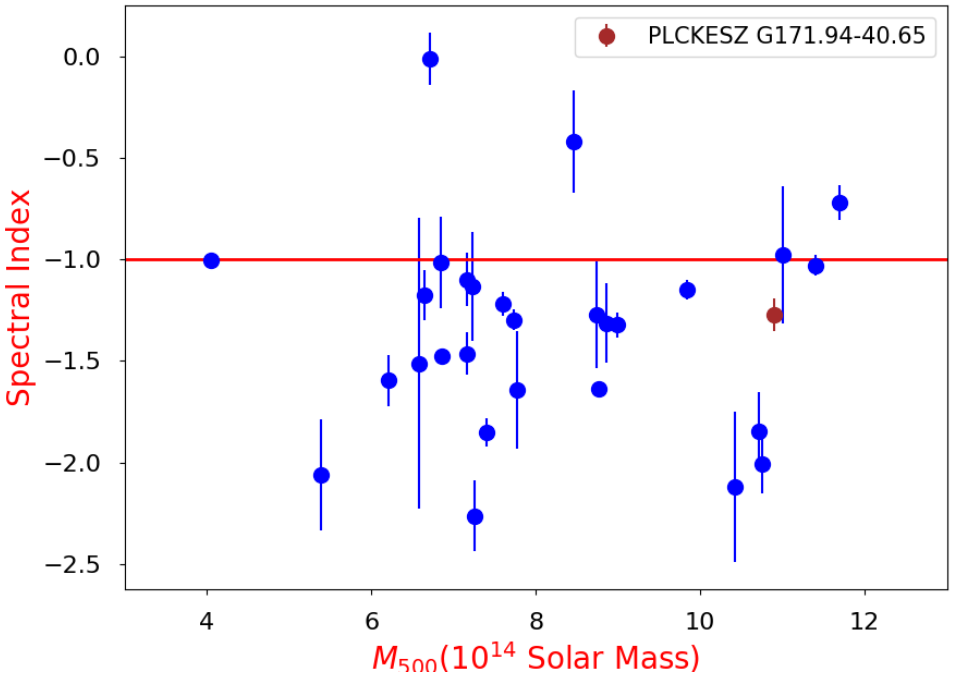

FIGURE 4.1: The radio halo spectral index versus the mass of the cluster are plotted. The cluster PLCKESZ G171.94-40.65 is marked with a red symbol and the rest of the sample is plotted with a blue symbol.

4.2.1 Spectral index versus Mass of the cluster using redshift as color code

The purpose of this statistical investigation is to see the correlation between the integrated spectral index and the mass of the cluster and its redshift. We have shown the variation of the spectral index α with mass of the cluster (M_{500}) Fig. 4.1. In Fig. 4.2 we plot the spectral index with mass and take the redshift as the parameter to generate the colour-map. We have not found any specific correlation or any specific trend of the cluster according to its redshift values. We point out that the clusters with highest redshift values in our sample (dark blue points) show steep spectrum i.e large negative values of the spectral index. However there are other low redshift clusters which also have steep spectra.

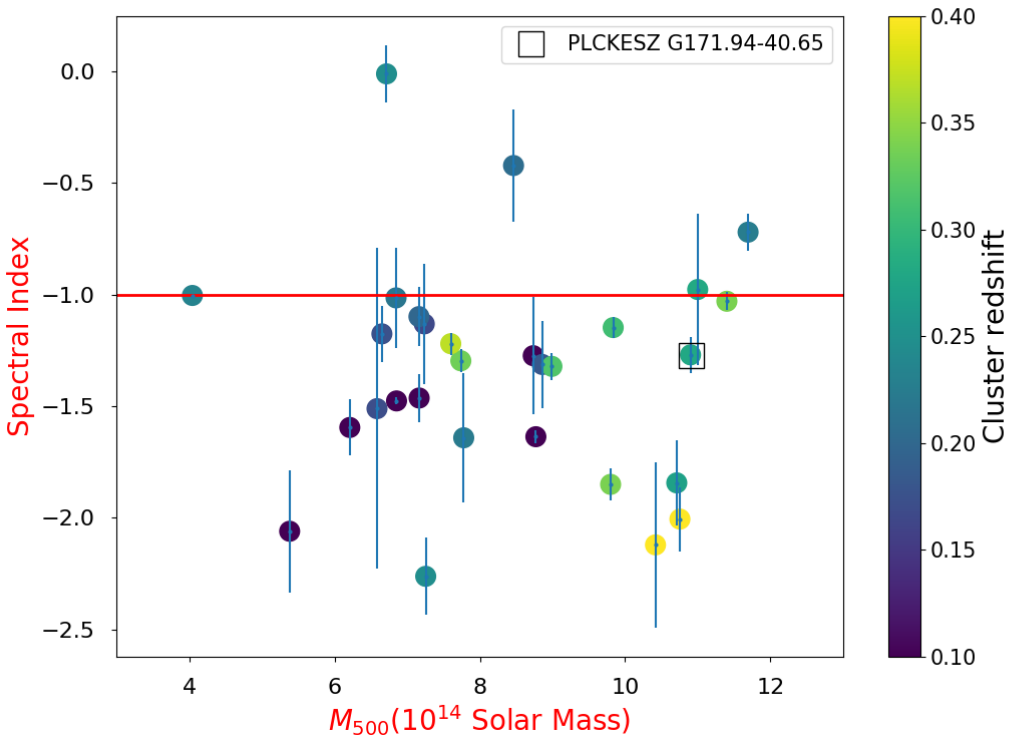

FIGURE 4.2: The spectral index versus the mass of the cluster with the color scale showing the redshift is plotted. The point for the cluster PLCKESZ G171.94-40.65 is highlighted with a square symbol.

4.3 Discussion

We assembled a sample of 89 radio halos from literature till date. We used a sub-sample of 33 radio halos for this study that had radio halo observations at more than one frequency. The statistical study tried to see any underlying connection among cluster mass, spectral index and redshift.

In Fig. 4.1 we have tried to see the any correlation between the spectral index and the mass of the cluster. The plot clearly shows that there is no correlation between these two parameters. Most of the sources shows spectra steeper than −1.0. Since we have limited size sample so any statistical conclusion cannot be drawn out of it. The absence of any trend indicates that the connection of the spectral index of the radio halo may be depending on the specific local condition of the cluster rather than a global dependence on mass. The efficiency of acceleration process and magnetic field amplification in mergers may be able to offset any trend due to

increased IC-losses as a function of redshift. We also note that the measurements at multiple radio frequencies to find the spectral indices may have short comings that can lead to uncertainties that will affect the trends in this plot.

We have shown the PLCKESZ G171.94-40.65 studied earlier. It is a giant radio halo with a typical spectral index like most the the radio halos.

4.4 Conclusions

- The statistical study is useful probe to investigate any correlation between the parameters of large scale diffuse sources. It has been observed that the mass of the galaxy cluster has positive correlation with the radio power. We used a sample of radio halos from literature available in van Weeren et al. (2019b) and complemented it with new discoveries after that. We have presented the new discoveries in this chapter.

- We have tried to see any correlation between the spectral index, the mass and redshift of the host cluster. We have not found any correlation though we are limited by our sample size.

- We also tried to see any trend according to the redshift of the cluster in Fig. 4.2 but did not observe any specific trend.

- The absence of trend can be interpreted in terms of the factors that are involved in the particle acceleration process that govern the spectral index. The global mass likely does not play a significant role in deciding the spectral index of the radio halo underlining that fact that radio halos are likely transient phenomena that are short lived as compared to cluster lifetime. Absence of a trend with redshift also indicates that the acceleration mechanism is able to offset the energy losses due to inverse-Compton scattering.

- Given the variety of telescopes and methods of measurements involved in arriving at the spectral indices of radio halos, there is likely a large uncertainty in it. Uniformity in methods needs to be brought in for carrying out measurements of flux density measurements of radio halos.

Chapter 5

Summary and conclusions

We started with the general introduction of the galaxy clusters followed by the radio band studies of the galaxy clusters and types of the diffuse extended emission in associated with these systems in Chapter 1. We then presented the motivation of the thesis which includes the radio studies of the clusters RXC J0528.9-3927 and PLCKG171.94-40.65. In Chapters 2 and 3 we presented these radio studies. In chapter 4 we have discussed the statistical study of the radio halos having observation at more than one frequency and tried to see any possible correlation of the spectral index of the halos, the mass and redshift of the cluster which host these sources. Following are the outcomes of the presented study:

- We have detected the presence of the radio diffuse emission in the galaxy cluster RXC J0528.9-3927 using GMRT observations at 610 MHz. The radio emission extends up to 272.6 kpc.
- Since we were limited by only one observation at 610 MHz, we then looked for the other surveys and found the total flux density for this source. The poor resolutions of the sources did not allow separation of the central radio source with the BCG and the extended part. We then assumed the BCG spectral index of the $\alpha = -0.75$ and assuming that total flux is the sum of extended and discrete source emission we found the flux density of the extended emission. Based on the above assumption we have found the spectral index of the extended emission is $\alpha = -1.9 \pm 07$ and we placed this source as steep spectrum source. We then calculated the cluster magnetic field for the cluster and found out it to be 1.09μG.

- We calculate the radio power for the cluster RXC J0528.9-3927 and compared this with existing sample of the mini-halos (Richard-Laferrière et al., 2020) and the radio power is highest in the sample.
- The extent of the diffuse emission and presence of the cold front in the cluster indicate that RXC J0528.9-27 is a radio mini halo, however deep observation may change the result.
- We also note the recent report of diffuse emission in this cluster by (Knowles et al., 2021) using MeerKAT and compare our results with theirs.
- We have detected the presence of the diffuse radio emission in the galaxy cluster PLCKG171.94-40.65 at the frequencies 235, 325, 610 and 1400 MHz using the GMRT and the VLA.
- We summarised the multi-frequency radio properties of the discrete radio sources in the cluster in Table. 3.1.
- We have calculated the integrated spectral index and magnetic field and radio power for the radio halo in galaxy cluster PLCKG171.94-40.65.
- We have discussed the method Halo-FDCA and compare its values of the flux density with CASA flux density values (Table. 3.5). However values from the method do not deviate much from the CASA flux density values. The integrated spectral index of for the diffuse radio halo is $\alpha = -1.27 \pm 0.08$ so this halo can not be considered as ultra steep spectrum diffuse source as suspected in earlier work.
- We also found the suspected relic in the periphery of the cluster with extent of the 74.5 kpc$\times$45.6 kpc. Right now we cannot decide the nature of this source and thus we have named it as a candidate relic.
- It has been observed that the mass of the galaxy clusters has positive correlation with the radio power. We have tried to see any correlation between the spectral index and the mass of the cluster and also with redshift. We have not found any correlation though we are limited by our sample size.
- We also tried to see any trend according to the redshift of the cluster in Fig. 4.2 but did not observe any specific trend but can loosely say that highest redshift clusters lie in the more steep spectra region.

- The absence of trends can be interpreted as the acceleration mechanism being driven by the properties of the merger and time elapsed. We also caution about the uncertainly introduced due to the variety of methods used to measure the total flux density and spectral indices of radio halos. The use of methods such as HALO-FDCA are thus necessary to bring in uniformity in measurements and undertake statistical studies.

Bibliography

Adam R., Goksu H., Brown S., Rudnick L., Ferrari C., 2021, A&A, 648, A60

Axford W. I., Leer E., Skadron G., 1977, in International Cosmic Ray Conference, Vol. 11, International Cosmic Ray Conference, p. 132

Bell A. R., 1978, MNRAS, 182, 443

Blandford R. D., Ostriker J. P., 1978, ApJ, 221, L29

Blasi P., Colafrancesco S., 1999, Astroparticle Physics, 12, 169

Botteon A., Gastaldello F., Brunetti G., 2018, MNRAS, 476, 5591

Boxelaar J. M., van Weeren R. J., Botteon A., 2021, Astronomy and Computing, 35, 100464

Brunetti G. et al., 2008, Nature, 455, 944

Brunetti G., Jones T. W., 2014a, International Journal of Modern Physics D, 23, 30007

Brunetti G., Jones T. W., 2014b, International Journal of Modern Physics D, 23, 1430007

Brunetti G., Setti G., Feretti L., Giovannini G., 2001, MNRAS, 320, 365

Carilli C. L., Taylor G. B., 2002, ARA&A, 40, 319

Cassano R., Brunetti G., Setti G., Govoni F., Dolag K., 2007, MNRAS, 378, 1565

Cassano R., Ettori S., Giacintucci S., Brunetti G., Markevitch M., Venturi T., Gitti M., 2010, ApJ, 721, L82

Condon J. J., Cotton W. D., Greisen E. W., Yin Q. F., Perley R. A., Taylor G. B., Broderick J. J., 1998, AJ, 115, 1693

Dennison B., 1980, ApJ, 239, L93

Deo D. K., Kale R., 2017, Experimental Astronomy, 44, 165

Di Gennaro G. et al., 2021, Nature Astronomy, 5, 268

Dolag K., Enßlin T. A., 2000, A&A, 362, 151

Donnert J., Dolag K., Brunetti G., Cassano R., 2013, MNRAS, 429, 3564

Enßlin T. A., Brüggen M., 2002, MNRAS, 331, 1011

Enßlin T. A., Gopal-Krishna, 2001, A&A, 366, 26

Feretti L., Giovannini G., Govoni F., Murgia M., 2012, AApR, 20, 54

Ferrari C., Govoni F., Schindler S., Bykov A. M., Rephaeli Y., 2008, Space Sci. Rev., 134, 93

Giacintucci S., Kale R., Wik D. R., Venturi T., Markevitch M., 2013, The Astrophysical Journal, 766, 18

Govoni F., Feretti L., 2004a, International Journal of Modern Physics D, 13, 1549

Govoni F., Feretti L., 2004b, International Journal of Modern Physics D, 13, 1549

Hoeft M. et al., 2020, arXiv e-prints, arXiv:2010.10331

Intema H. T., Jagannathan P., Mooley K. P., Frail D. A., 2017, A&A, 598, A78

Kale R., Ishwara-Chandra C. H., 2021, Experimental Astronomy, 51, 95

Kale R., Shende K. M., Parekh V., 2019, MNRAS, 486, L80

Kale R. et al., 2015, A&A, 579, A92

Kale R., Venturi T., Giacintucci S., Dallacasa D., Cassano R., Brunetti G., Macario G., Athreya R., 2013, A&A, 557, A99

Knowles K. et al., 2021, MNRAS, 504, 1749

Krymskii G. F., 1977, Akademiia Nauk SSSR Doklady, 234, 1306

Loewenstein M., 2004, in Origin and Evolution of the Elements, McWilliam A., Rauch M., eds., p. 422

Malkov M. A., Drury L. O., 2001, Reports on Progress in Physics, 64, 429

Mauch T., Murphy T., Buttery H. J., Curran J., Hunstead R. W., Piestrzynski B., Robertson J. G., Sadler E. M., 2003, MNRAS, 342, 1117

Murgia M., Govoni F., Markevitch M., Feretti L., Giovannini G., Taylor G. B., Carretti E., 2009, A&A, 499, 679

Perley R. A., Butler B. J., 2017, ApJS, 230, 7

Planck Collaboration et al., 2014, A&A, 571, A29

Planck Collaboration et al., 2011a, A&A, 536, A1

Planck Collaboration et al., 2011b, A&A, 536, A8

Raja R. et al., 2020, MNRAS, 493, L28

Richard-Laferrière A. et al., 2020, MNRAS, 499, 2934

Rossetti M., Gastaldello F., Eckert D., Della Torre M., Pantiri G., Cazzoletti P., Molendi S., 2017, MNRAS, 468, 1917

Sarazin C. L., 1986, Reviews of Modern Physics, 58, 1

Schlickeiser R., Sievers A., Thiemann H., 1987, A&A, 182, 21

Sunyaev R. A., Zeldovich Y. B., 1972, Comments on Astrophysics and Space Physics, 4, 173

van Weeren R. J., de Gasperin F., Akamatsu H., Brüggen M., Feretti L., Kang H., Stroe A., Zandanel F., 2019a, Space Sci. Rev., 215, 16

van Weeren R. J., de Gasperin F., Akamatsu H., Brüggen M., Feretti L., Kang H., Stroe A., Zandanel F., 2019b, Space Sci. Rev., 215, 16

Venturi T., Giacintucci S., Brunetti G., Cassano R., Bardelli S., Dallacasa D., Setti G., 2007, A&A, 463, 937

Venturi T., Giacintucci S., Dallacasa D., Cassano R., Brunetti G., Bardelli S., Setti G., 2008, A&A, 484, 327

Wilner D. J., Welch W. J., 1994, ApJ, 427, 898

Xie C. et al., 2020, A&A, 636, A3

Zhang C., Yu Q., Lu Y., 2014, ApJ, 796, 138

ZuHone J., Brunetti G., Giacintucci S., Markevitch M., 2014, ArXiv e-prints